J. Fluid Mech. (2013), *vol.* 720, *pp.* 357–392.
doi:10.1017/jfm.2013.37

Rogue wave occurrence and dynamics by direct simulations of nonlinear wave-field evolution

Wenting Xiao, Yuming Liu, Guangyu Wu‡ and Dick K. P. Yue†

Department of Mechanical Engineering, Massachusetts Institute of Technology, Cambridge, MA 02139, USA

(Received 20 September 2012; revised 7 December 2012; accepted 14 January 2013; first published online 27 February 2013)

We study the occurrence and dynamics of rogue waves in three-dimensional deep water using phase-resolved numerical simulations based on a high-order spectral (HOS) method. We obtain a large ensemble of nonlinear wave-field simulations ($M = 3$ in HOS method), initialized by spectral parameters over a broad range, from which nonlinear wave statistics and rogue wave occurrence are investigated. The HOS results are compared to those from the broad-band modified nonlinear Schrödinger (BMNLS) equations. Our results show that for (initially) narrow-band and narrow directional spreading wave fields, modulational instability develops, resulting in non-Gaussian statistics and a probability of rogue wave occurrence that is an order of magnitude higher than linear theory prediction. For longer times, the evolution becomes quasi-stationary with non-Gaussian statistics, a result not predicted by the BMNLS equations (without consideration of dissipation). When waves spread broadly in frequency and direction, the modulational instability effect is reduced, and the statistics and rogue wave probability are qualitatively similar to those from linear theory. To account for the effects of directional spreading on modulational instability, we propose a new modified Benjamin–Feir index for effectively predicting rogue wave occurrence in directional seas. For short-crested seas, the probability of rogue waves based on number frequency is imprecise and problematic. We introduce an area-based probability, which is well defined and convergent for all directional spreading. Based on a large catalogue of simulated rogue wave events, we analyse their geometry using proper orthogonal decomposition (POD). We find that rogue wave profiles containing a single wave can generally be described by a small number of POD modes.

Key words: surface gravity waves, waves/free-surface flows

1. Introduction

Rogue waves are extraordinarily large surface waves that appear infrequently in the ocean. A common definition of rogue waves is waves whose heights exceed twice the significant wave height. Occurrences of such large waves have been reported worldwide from ships, offshore platforms and radars (Lawton 2001; Kharif & Pelinovsky 2003; Forristall 2005). Collisions with such waves have caused catastrophic

† Email address for correspondence: yue@mit.edu

‡ Present address: Chevron Energy Technology Company, 1400 Smith Street, Houston, TX 77002, USA.

damage to ships and offshore structures (Kharif & Pelinovsky 2003; Toffoli *et al.* 2005). Recent reviews of the rogue wave problem may be found in Kharif & Pelinovsky (2003), Dysthe, Krogstad & Muller (2008), Kharif, Pelinovsky & Slunyaev (2009) and Slunyaev, Didenkulova & Pelinovsky (2011).

The prediction of the occurrence probability of rogue waves is of central interest. In linear random wave theory, the wave field is considered as a superposition of sinusoidal wave components with different frequencies and directions of propagation, and the surface is described by a Gaussian distribution. Under this assumption, Longuet-Higgins (1952) shows that, for unidirectional waves that are narrow-band in frequency, wave height and thus rogue wave occurrence follow a Rayleigh distribution. This linear theory is extended to include second-order bound wave effects (Tayfun 1980; Forristall 2000). The inclusion of second-order nonlinearity leads to sharper crests and flatter troughs, with improved statistical comparison to field measurements, although the crest-to-trough wave height remains the same. Significantly, observations indicate that the classical linear and second-order theories do not properly describe the occurrence of large waves with heights greater than twice the significant wave height (Skourup, Hansen & Andreasen 1997; Stansell 2005).

The enhanced occurrence probability of large waves can be due to a number of physical mechanisms (Kharif & Pelinovsky 2003). In addition to superposition of dispersive waves with proper frequency and phase combinations, linear mechanisms associated with wave refraction by variable current or bottom topography have been proposed (Lavrenov 1998). When nonlinearity is present, significant interactions occur at the third order, and it is postulated that nonlinear focusing due to modulational instability (MI) is an important generation mechanism of rogue waves. It is known that an initially periodic Stokes wave train is unstable to sideband modulations (Benjamin & Feir 1967), causing the wave train to disintegrate into wave groups within which large waves could form. This type of Benjamin–Feir MI also occurs in narrow-band irregular wave fields (Alber 1978), and its relationship to rogue wave formation has been studied theoretically, experimentally and numerically.

For unidirectional narrow-band seas, Janssen (2003) shows theoretically that MI can cause an exponential growth of the central wave mode, leading to the formation of large waves, and the importance of MI can be measured by the Benjamin–Feir index (BFI), which is the ratio of the wave-field steepness to the spectral bandwidth. By including the third-order nonlinearity of MI, the wave height follows the modified Edgeworth–Rayleigh (MER) distribution, which involves the fourth-order moment or kurtosis of the surface elevation (Mori & Yasuda 2002; Mori & Janssen 2006). The MER distribution deviates from the Rayleigh distribution and predicts increasing probability of rogue waves with increasing kurtosis. In the special case when the wave field is described by a very narrow-band Gaussian spectrum, kurtosis is specified by the value of the BFI (Mori & Janssen 2006). In wave flume experiments, strongly non-Gaussian values of kurtosis and enhanced occurrence of large waves are observed in wave fields with large wave steepness and narrow-band initial wave spectrum (corresponding to large BFI), which supports the suggestion that MI plays an important role in the occurrence of large waves during nonlinear wave evolution (Onorato *et al.* 2004; Shemer & Sergeeva 2009; Shemer, Sergeeva & Liberzon 2010*a*).

For computational efficiency, many existing numerical studies use model equations based on the wave envelope approximation (assuming narrow-band waves), such as nonlinear Schrödinger (NLS) or modified nonlinear Schrödinger (MNLS) equations and their extended forms, to allow slightly broad-band spectrum (broad-band modified nonlinear Schrödinger equations, BMNLS) (Dysthe 1979; Trulsen & Dysthe 1996).

Using one-dimensional NLS simulations, the possible connection between MI and rogue wave occurrence is confirmed by Onorato *et al.* (2001). Another type of weakly nonlinear model is the one based on Zakharov's integro-differential equation, which includes broad-band wave interactions (Shemer, Kit & Jiao 2002; Annenkov & Shrira 2009*a*). A few attempts have also been made to obtain fully nonlinear simulations for the evolution of unidirectional waves (Zakharov, Dyachenko & Vasilyev 2002; Chalikov 2009; Slunyaev & Sergeeva 2011). In particular, Chalikov (2009) also finds a strong correlation between the kurtosis and rogue wave occurrence.

For general three-dimensional (3D) wave fields with broad directional spreading, statistical theory accounting for nonlinearity is difficult to obtain, and much of the investigation is based on experimental and numerical simulations. It is found in wave basin experiments that the increase of spreading angles can lead to a significant reduction of kurtosis and occurrence of rogue waves (Stansberg 1994; Onorato *et al.* 2009; Waseda, Kinoshita & Tamura 2009). This is confirmed by numerical simulations based on NLS-type models, where it is found that the importance of MI is reduced with decreasing crest length, and, for broad directional wave fields, the probability of rogue wave occurrence is close to Gaussian statistics and nearly independent of BFI (Onorato, Osborne & Serio 2002; Gramstad & Trulsen 2007). To account for the effect of directional spreading on rogue wave occurrence in 3D wave fields, different modified BFI parameters are proposed based on wave tank experiments (Waseda *et al.* 2009) and NLS simulations (Mori, Onorato & Janssen 2011). Fully nonlinear simulations are also developed, but are generally applied in a small wave field (Bateman, Swan & Taylor 2001; Ruban 2011).

NLS-type simulations are potentially limited by the inherent assumptions of narrow-band spectrum and slowly varying spatial and temporal modulations. These assumptions may not hold in general, since it is known that even an initially narrow-band spectrum may become broad-band due to nonlinear evolution (Dysthe *et al.* 2003). For steep waves (which might be expected in rogue wave events), the assumption of slowly varying modulation may also be invalid locally. One of the objectives of the present work is to assess the range of validity of wave envelope models for rogue wave predictions in directional wave fields over the MI scales. This is addressed in the recent study of Toffoli *et al.* (2010), where BMNLS theory simulation is compared with direct simulation using a high-order spectral (HOS) method (Dommermuth & Yue 1987; West *et al.* 1987). Toffoli *et al.* (2010) show that the BMNLS equations and the HOS method give qualitatively similar results, which compare reasonably with the wave tank experiments of Onorato *et al.* (2009). The simulations are, however, limited to relatively short evolution time (suggested by the scale of the tank experiments) and small computational domains.

In the present work, we apply direct numerical simulations to study the generation mechanisms and occurrence probability of rogue waves in 3D wave fields based on the HOS method developed in Dommermuth & Yue (1987). Our focus is on the importance of MI as a generation mechanism of rogue waves over space and time scales $\mathscr{L} \times \mathscr{L}$ and $\mathscr{T}$, with $\mathscr{L}/\lambda_p, \mathscr{T}/T_p \sim O(\varepsilon^{-2})$, where λ_p and T_p are the peak wavelength and period of the (initial) spectrum. Here $\varepsilon = H_s k_p/2$ is the steepness of the wave field, where H_s is the significant wave height and k_p is the peak wavenumber. Note that $\mathscr{T}/T_p \sim O(\varepsilon^{-2})$ is still shorter than the kinetic scale $O(\varepsilon^{-4})$. Longer evolution up to the kinetic scale is considered in Annenkov & Shrira (2009*a*,*b*) and Slunyaev & Sergeeva (2011). Our objectives are to obtain the occurrence probability, mechanisms and geometry of rogue wave events and their quantification in terms of statistical and spectral parameters. To achieve this, we perform a significant number

of large-scale nonlinear 3D HOS simulations covering a broad range of spectral parameters. The spatial and temporal scales of the simulations are commensurate with those of quartet resonance interactions, including Benjamin–Feir type instabilities; and sufficient realizations are obtained where needed to obtain convergent statistics. The simulations are performed on massively parallel high-performance computing (HPC) platforms. To account for natural dissipation due to wave breaking during the evolution, we implement a robust phenomenologically based model in HOS, which obtains satisfactory wave breaking dissipation for 2D and 3D breaking compared to laboratory measurements. For the spatial–temporal scales considered in this study, the growth of waves due to wind input is practically insignificant (Dysthe *et al.* 2003; Janssen 2003). We thus ignore the wind effect. In this initial study, we further assume deep water, and ignore the bottom and current, although these effects have been included in HOS (Dommermuth & Yue 1988; Liu & Yue 1998). For comparison, we also implement BMNLS and compare HOS and BMNLS model predictions over the large-scale space–time domains we consider.

For this study, a total of $O(200)$ 3D HOS wave fields are obtained (in the 'MIT-Wave' database). The HOS wave fields are initially described by a Joint North Sea Wave Project (JONSWAP) spectrum with cosine-squared spreading function, with wave steepness $\varepsilon = 0.06$–0.14, spectral bandwidth (controlled by peak enhancement parameter) $\gamma = 1$–10 and spreading angle $\Theta = 20$–120°. Using the MIT-Wave database, we characterize the nonlinear wave-field evolutions, and identify and collect the large wave events from which occurrence probabilities, rogue wave geometries (as well as rogue wave kinematics and dynamics, not presented here) are obtained, all as functions of spectral parameters.

In quantifying the dependence of nonlinear wave statistics and rogue wave probability on spectral parameters, we elucidate the similarities and differences between HOS and BMNLS predictions and the range of validity of the latter in terms of the spectral frequency bandwidth and directional spreading. For initially narrow-band and narrow directional spreading wave fields, MI leads to significant frequency and directional broadening, non-Gaussian statistics and enhanced rogue wave occurrence over a time scale $t/T_p \lesssim O(\varepsilon^{-2})$. This is observed in both HOS and BMNLS, although BMNLS appreciably overpredicts the frequency and directional broadening as well as the kurtosis, probably related to the narrow-band assumption in BMNLS. After longer evolution, $t/T_p \gtrsim O(\varepsilon^{-2})$, the HOS wave field obtains a quasi-stationary state (without significant further spreading in frequency and direction) that is distinctly non-Gaussian (as measured by, say, the kurtosis). This is not predicted by BMNLS, in which spectral broadening in frequency and direction continues, and the wave field eventually reaches an asymptotic almost-Gaussian state within which nonlinearity plays a minimal role. For an initially broad directional spreading spectrum, MI plays a minor role over these time scales, and relatively small spectral evolution and almost-Gaussian statistics obtain. These are predicted by both HOS and BMNLS, although the latter still generally overpredicts the frequency and directional broadening. Since our interest is in rogue wave occurrence, and specifically deviations from Gaussian–Rayleigh predictions due to MI, the above findings suggest the importance and usefulness of HOS over the MI time scale ($t/T_p = O(\varepsilon^{-2})$) considered in this study.

Using HOS simulations, we confirm the close correlation between rogue wave occurrence probability and kurtosis (Mori & Janssen 2006) for a broad range of spectral steepness, frequency bandwidth and directional spreading. For unidirectional narrow-band waves, kurtosis is in turn closely correlated with the BFI of the (initial)

spectrum (Mori & Janssen 2006). For broad directional spreading wave fields, BFI is no longer a sufficient measure of the importance of MI. We propose a new modified Benjamin–Feir index (MBFI) for general 3D wave fields, as a useful spectral parameter for predicting the effect of MI on kurtosis and the occurrence of rogue waves.

Occurrence probability has traditionally been defined as the ratio of the number of rogue waves to the total number of waves in a given wave field. This number probability (P_N) definition is less useful in broad-band and broad directional spreading seas where the estimation of the number of waves becomes problematic. The situation is exasperated since initially narrow-band, narrow-spreading seas tend towards spectra broad in frequency and direction due to MI. We introduce an area probability (P_A) for rogue wave occurrence for general directional seas. Probability P_A approaches P_N for waves narrow in frequency and spreading angle, but obtains meaningful estimates of the likelihood of rogue waves for broad directional spreading wave fields.

HOS simulations not only indicate the presence of rogue wave events but also provide the detailed geometry and kinematics of such waves. Thus MIT-Wave can be used to catalogue and study the geometric structures of rogue waves and their dependence on the underlying wave spectra. We obtain dominant geometrical structures of rogue waves using proper orthogonal decomposition (POD). We find that 2D and 3D rogue waves containing a single main wave can generally be represented using only a few POD modes.

The paper is organized as follows. In § 2, a phase-resolved numerical model for large-scale nonlinear wave-field evolution based on HOS is described. In § 3 we compare the spectral evolution and nonlinear wave statistics calculated from HOS and BMNLS simulations. The number and area probability of rogue waves as functions of statistical and spectral parameters are quantified and shown in § 4. In § 5, we analyse the geometrical structures of rogue waves identified and collected from MIT-Wave using POD. Conclusions and discussions are given in § 6.

2. Numerical simulation of nonlinear wave fields

We consider three-dimensional deep-water wave fields described by spectral parameters covering a broad range of frequency, spectral bandwidth, directional spreading angle and wave steepness. We simulate large spatial domains $\mathscr{L} \times \mathscr{L}$ and evolution times $\mathscr{T}$ given by $\mathscr{L}/\lambda_p, \mathscr{T}/T_p \sim O(\varepsilon^{-2})$. These scales are consistent with those required for significant third-order MI effects to change the wave fields. Selective simulations are performed using both HOS and BMNLS models, which allow us to obtain direct quantitative comparisons.

2.1. *Direct simulation using high-order spectrum method (HOS)*

2.1.1. *Formulation and numerical approach*

We perform phase-resolved simulations of large-scale nonlinear wave fields in the context of potential flow based on an HOS method (Dommermuth & Yue 1987; West *et al.* 1987). HOS directly solves the field equation with the kinematic and dynamic boundary conditions on the free surface in the Zakharov form:

$$\eta_t - \Phi_z = -\eta_{\boldsymbol{x}} \cdot \Phi^S_{\boldsymbol{x}} + (\eta_{\boldsymbol{x}} \cdot \eta_{\boldsymbol{x}})\Phi_z \quad \text{at } z = \eta(\boldsymbol{x}, t), \tag{2.1a}$$

$$\Phi^S_t + g\eta = -\tfrac{1}{2}(\Phi^S_{\boldsymbol{x}} \cdot \Phi^S_{\boldsymbol{x}}) - \tfrac{1}{2}(1 + \eta_{\boldsymbol{x}} \cdot \eta_{\boldsymbol{x}})\Phi^2_z \quad \text{at } z = \eta(\boldsymbol{x}, t), \tag{2.1b}$$

where $\boldsymbol{x} = (x, y)$ and z are the horizontal and vertical coordinates, $\Phi(\boldsymbol{x}, z, t)$ is the velocity potential and $\Phi^S(\boldsymbol{x}, t) \equiv \Phi(\boldsymbol{x}, z = \eta(\boldsymbol{x}, t), t)$ is the value of the potential on the free surface $\eta(\boldsymbol{x}, t)$.

In HOS, nonlinear interactions among a large number of wave components, $N = N_x \times N_y$, are accounted for up to arbitrary order M in wave steepness. The computational effort is approximately linear in N and M, with exponential convergence with M and N for waves up to ~80 % of Stokes limiting steepness. The validity and efficacy of this method have been demonstrated extensively for nonlinear wave–wave interactions (Dommermuth & Yue 1987), and the method has been extended to include atmospheric forcing (Dommermuth & Yue 1988), variable finite depth (Liu & Yue 1998) and effects of energy dissipation (Wu, Liu & Yue 2006). In this work, a robust phenomenologically based model is implemented in HOS to account for energy dissipation due to wave breaking (§ 2.1.2).

For the present study involving very large-scale ($N = O(10^{7\text{–}8})$) simulations, we develop a parallelized version of HOS optimized for modern massively parallel HPC platforms, using Message Passing Interface (MPI) functions (Wu 2004). Our experience with parallelized HOS using up to $\mathscr{P} = O(10^3)$ Cray XT3 and XT4 processors indicates near linear scaling of HPC time with $\mathscr{P}^{-1}$. For simulations with $N = O(10^7)$ and $M = O(4)$, for example, the required time on HPC with $\mathscr{P}$ processors is $O(0.5)/\mathscr{P}$ hours per HOS time step.

In this study, we typically use a computational domain $L_x \times L_y = 128\lambda_p \times 128\lambda_p$ with doubly periodic boundary conditions; $N_x \times N_y = 4096 \times 4096$ free wave modes (before de-aliasing); fourth-order Runge–Kutta time integration with $\Delta t = T_p/32$; and order of nonlinearity $M = 3$ to capture the third-order nonlinearity in the MI. We perform extensive convergence tests varying the values of $L_{x,y}/\lambda_p$, N_x, N_y, Δt and M. With the parameters we choose, the statistics we report of a *given* nonlinear wave field are converged to ~0.5 % for total energy, and to ~1 % for skewness and kurtosis. In many of our results, we further perform ensemble averaging over multiple (typically $O(10)$) realizations (of the same conditions) to obtain statistically useful results of the extreme events. Aggregating these realizations, we obtain typically $N_{rogue} = O(10^2)$ rogue wave events from which extreme statistics are obtained.

2.1.2. *Modelling energy dissipation due to wave breaking*

For the large-scale long-time simulations that we consider, it is important to account for energy loss associated with wave breaking dissipation in the evolution. The detailed mechanism and dynamics of different types of (2D and 3D) breaking events is a big topic beyond the scope of this study. It is however possible to capture the effect of wave breaking dissipation on the overall wave-field evolution using relatively simple phenomenological models in HOS.

For different types of spilling or plunging breaking waves in the laboratory and field, it is observed that the energy dissipation is generally confined in the high frequency or wavenumber range of the wave spectrum (Rapp & Melville 1990; Gemmrich & Farmer 1999). Based on this, we propose an energy dissipation model in HOS, where a low-pass filter in the wavenumber space is applied at every time step on the free surface elevation and velocity potential. An example of such a filter is

$$\Lambda(\boldsymbol{k} \mid k_p, \beta_1, \beta_2) = \exp\left(-\left|\frac{k}{\beta_1 k_p}\right|^{\beta_2}\right), \tag{2.2}$$

where $k = |\boldsymbol{k}|$ with $\boldsymbol{k} = (k_x, k_y)$ and β_1 and β_2 are filter parameters.

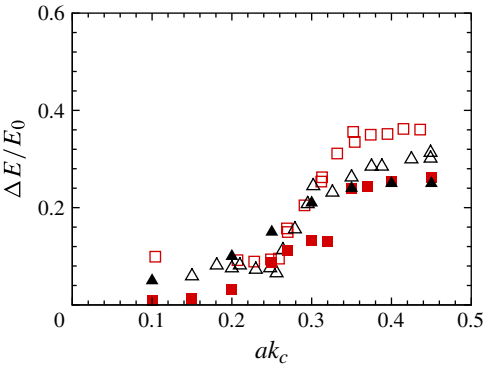

FIGURE 1. (Colour online) Loss of energy due to wave breaking as a function of steepness of the dispersive wave packet ak_c. Experiments (Rapp & Melville 1990): $f_c = 0.88$ (□) and 1.08 (△). HOS: $f_c = 0.88$ (■) and 1.08 (▲). Here f_c and k_c are the central frequency and wavenumber of a dispersive wave packet. Results are obtained using HOS with (2.2) with $\beta_1 = 8$, $\beta_2 = 30$.

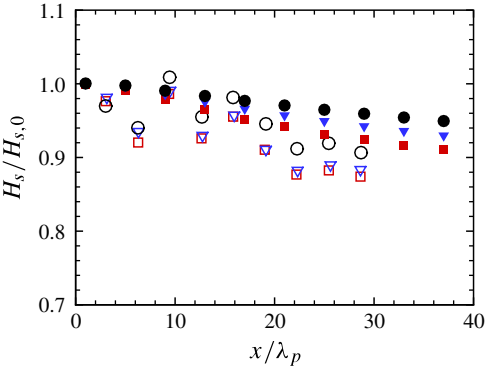

FIGURE 2. (Colour online) Spatial variation of significant wave height H_s scaled by its initial value for wave fields initially given by the JONSWAP spectrum with $\varepsilon = 0.16$, $\gamma = 6$, with a range of spreading angles. Experiment (Onorato *et al.* 2009): $\Theta = 12°$ (□), 21° (▽) and 62° (○). HOS: $\Theta = 12°$ (■), 21° (▼) and 62° (●). Results are obtained using HOS with (2.2) with $\beta_1 = 8$, $\beta_2 = 30$.

The model (2.2) is found to be robust for a variety of 2D and 3D wave fields in that the estimate of energy dissipation is found to be somewhat insensitive to the choice of parameter values β_1 and β_2 (or in some sense the specific form of (2.2)). This is confirmed by repeated simulations varying (the parameters of) (2.2), for example, varying $\beta_1 = 7$–8 and $\beta_2 = 20$–35, the total energy variation is within 2 % at evolution time $t = 150T_p$.

The efficacy of this modelling has been confirmed by direct comparisons against 2D and 3D measurements – see Wu (2004) and Xiao (2013) for details. Based on these validations, we typically use (2.2) with fixed values of $\beta_1 = 8$ and $\beta_2 = 30$ in all large-scale HOS simulations. For an example of two-dimensional breaking waves, figure 1 shows the energy loss measured from laboratory breaking dispersive wave packets as a function of wave packet steepness (Rapp & Melville 1990) compared with HOS predictions. An acceptable quantitative agreement is found over a broad range of steepnesses (and corresponding breaking types). Figure 2 shows an example from 3D

breaking waves where the spatial variation of significant wave height H_s ($=4\sigma$, where σ is the standard deviation of the wave surface) due to breaking in a 3D random wave field is measured (Onorato *et al.* 2009). The HOS simulations (using the same dissipation model and parameters) again obtain satisfactory agreements over the range of directional spreading reported.

2.2. *Modified nonlinear Schrödinger equations*

We implement the modified nonlinear Schrödinger equations, which allow slightly broader bandwidth (BMNLS) (Dysthe 1979; Trulsen & Dysthe 1996) to assess the range of validity in describing nonlinear wave statistics and rogue wave probability over the present large-scale spatial and temporal domains $\mathscr{L}/\lambda_p$, $\mathscr{T}/T_p \sim O(\varepsilon^{-2})$. The BMNLS model (to fourth order in wave steepness) describes the evolution of the wave envelope $B(\boldsymbol{x}, t)$, which is slowly varying with space and time. Wave breaking is generally not considered in NLS-type models (Dysthe *et al.* 2003; Socquet-Juglard *et al.* 2005), although the effect of dissipation can be included (see e.g. Segur *et al.* 2005). After $B(\boldsymbol{x}, t)$ is solved, the surface elevation is reconstructed as

$$\eta(\boldsymbol{x}, t) = \overline{\eta} + \tfrac{1}{2}(B\mathrm{e}^{\mathrm{i}\theta} + B_2\mathrm{e}^{2\mathrm{i}\theta} + B_3\mathrm{e}^{3\mathrm{i}\theta} + \cdots + \text{c.c.}), \tag{2.3}$$

where B_2, B_3 and $\overline{\eta}$, obtained from B, represent corrections of second and third harmonics and the mean surface elevation associated with the radiation stress, and $\theta = \boldsymbol{k}_p \cdot \boldsymbol{x} - \omega_p t$ is the phase of the peak wave.

We solve the BMNLS model numerically using the split-step Fourier method described in Lo & Mei (1985). The envelope function $B(\boldsymbol{x}, t)$ is solved in the modulational wavenumber space $\boldsymbol{K} = (K_x, K_y) = (\boldsymbol{k} - \boldsymbol{k}_p)/k_p$ and only the modes within $|K_x| \leqslant 1$ and $|K_y| \leqslant 1$ are used. This is slightly different from Socquet-Juglard *et al.* (2005), in which the modes within $|\boldsymbol{K}| \leqslant 1$ are used. The computational domain is $128\lambda_p \times 128\lambda_p$, over which a uniform grid size $N_x = N_y = 512$ is applied. To resolve the rapidly oscillating surface elevation, $\eta(\boldsymbol{x}, t)$, a uniform grid size of 4096×4096 is used. These computational parameter values result in identical spatial and spectral discretization with the HOS simulations. For all the BMNLS simulations, the energy is verified to be conserved to within $\sim$0.5 %. The present BMNLS solver has been systematically validated through convergence tests (see figure 8) and direct comparisons with various existing results in the literature (Lo & Mei 1985; Dysthe *et al.* 2003; Socquet-Juglard *et al.* 2005; Toffoli *et al.* 2011) and the HOS simulations.

2.3. *Specifying the initial random directional wave field*

The initial wave field is specified by the JONSWAP spectrum with a directional spreading function

$$S(\omega, \theta) = \frac{\alpha_p g^2}{\omega^5}\exp\left[-\frac{5}{4}\left(\frac{\omega}{\omega_p}\right)^{-4}\right]\gamma^{\exp[-(\omega-\omega_p)^2/(2\sigma^2\omega_p^2)]}D(\theta), \tag{2.4}$$

where ω is the wave frequency, ω_p the peak wave frequency, α_p the Phillips parameter, γ the peak enhancement factor specifying the spectral bandwidth, and $\sigma = 0.07$ for $\omega \leqslant \omega_p$ and $\sigma = 0.09$ for $\omega > \omega_p$.

The directional spreading is given by a cosine-squared function:

$$D(\theta) = \begin{cases} \dfrac{2}{\Theta}\cos^2\left(\dfrac{\pi\theta}{\Theta}\right) & \text{for } |\theta| \leqslant \Theta/2, \\ 0 & \text{for } |\theta| > \Theta/2, \end{cases} \tag{2.5}$$

where θ is the wave propagation direction and Θ is the directional spreading width. The corresponding directional wavenumber spectrum is given by $\Psi(\boldsymbol{k}) = g^2/(2\omega^3)S(\omega, \theta)$, where $\boldsymbol{k} = (k_x, k_y)$ is the wavenumber vector.

To elucidate the case of a very narrow-band Gaussian spectrum considered by Alber (1978) and Dysthe *et al.* (2003), we also perform HOS and BMNLS simulations for wave fields specified by a Gaussian wavenumber spectrum:

$$\Psi(\boldsymbol{k}) = \frac{\sigma^2}{2\pi\delta_k^2} \exp\left[-\frac{1}{2k_p^2}\left(\frac{(k_x - k_p)^2}{\delta_k^2} + \frac{k_y^2}{\delta_k^2}\right)\right], \tag{2.6}$$

where $\sigma = \left(\int \Psi(\boldsymbol{k})\,\mathrm{d}\boldsymbol{k}\right)^{1/2}$ is the standard deviation of the surface elevation, k_p the peak wavenumber, and δ_k the spectral bandwidth in the x and y directions.

For HOS realization, the initial wave field is constructed from linear superposition of wave components with amplitude

$$a(\boldsymbol{k}) = \mathrm{Re}\left\{\sqrt{2\Psi(\boldsymbol{k})\Delta k_x \Delta k_y}\exp(\mathrm{i}\psi)\right\}, \tag{2.7}$$

where the phase ψ is a random variable uniformly distributed over $[0, 2\pi]$. To minimize initial transients in the numerics, the nonlinear terms in (2.1) are ramped up smoothly from zero over several ($\sim O(5)$) T_p (Dommermuth 2000). Similarly, BMNLS computations are initialized by specifying the complex amplitude of the wave envelope:

$$B(\boldsymbol{K}) = \sqrt{2\Psi(\boldsymbol{K})\Delta K_x \Delta K_y}\exp(\mathrm{i}\psi). \tag{2.8}$$

3. Spectral evolution and nonlinear wave statistics

3.1. *Spectrum evolution: HOS versus BMNLS*

We first consider the very narrow-band Gaussian spectrum (2.6), which is unstable if $\delta_k < 2\varepsilon$, where $\varepsilon = \sqrt{2}\sigma k_p$ (Alber 1978). This is assessed in Dysthe *et al.* (2003) using BMNLS simulations, where they report a spectral broadening during wave-field evolution regardless of the initial spectral bandwidth for three-dimensional wave fields. We investigate the evolution of the very narrow-band Gaussian spectrum using HOS simulations, comparing it to BMNLS predictions. Figure 3 shows the spectral evolution from BMNLS and HOS simulations for the very narrow-band Gaussian spectrum with $\varepsilon = 0.1$ and $\delta_k = 0.1$. The spectra presented, which are obtained by ensemble averaging over five realizations, are smoothed by the use of five-point smoothing in both the k_x and k_y directions. HOS and BMNLS give similar predictions for the features of spectral change, including significant spectral widening and spectral peak downshifting. At longer times $t > 100T_p$, and especially for the short waves, however, BMNLS simulations obtain slightly broader directional spreading. The spectral evolution for $\varepsilon = 0.1$ and $\delta_k = 0.2$ is shown in figure 4. A similar broadening of the spectrum is observed in both BMNLS and HOS simulations, although the overall broadening process is slower and less significant in this case. BMNLS simulations again predict a broader spectrum at large times in comparison with HOS simulations. Based on both simulations, the Gaussian spectrum changes in three-dimensional wave field and more significantly so when the instability condition $\delta_k < 2\varepsilon$ is satisfied. These are reasonably well predicted by both HOS and BMNLS simulations with minor quantitative differences.

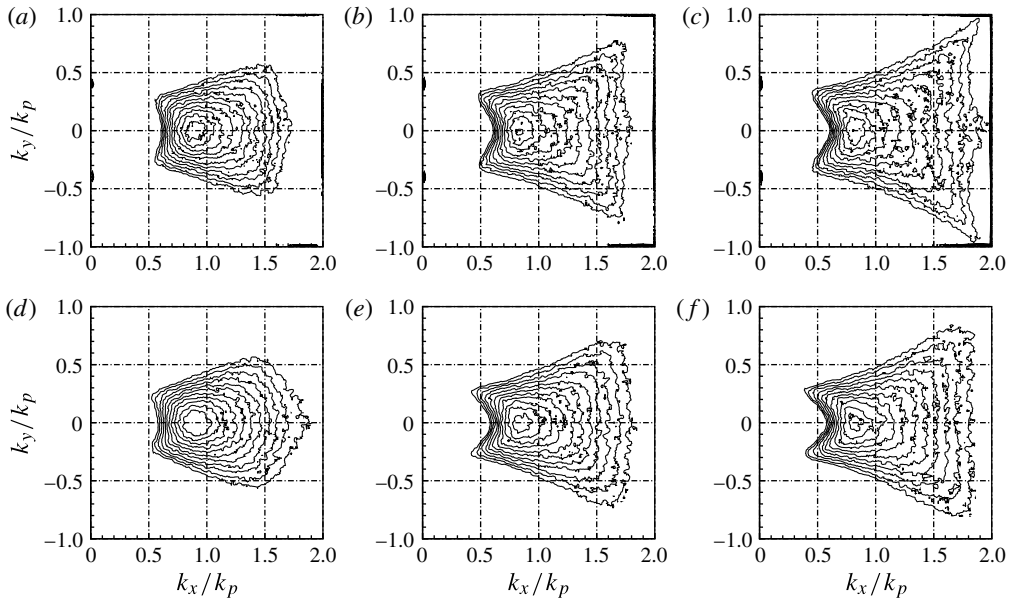

FIGURE 3. Evolution of the wavenumber spectrum $\Psi(\boldsymbol{k})$ of initially very narrow-band Gaussian spectrum (2.6) with $\varepsilon = 0.1$ and $\delta_k = 0.1$: (*a–c*) BMNLS; (*d–f*) HOS; (*a*,*d*) $t = 50T_p$; (*b*,*e*) $t = 100T_p$; (*c*,*f*) $t = 150T_p$. The contour values are logarithmic, ranging from 1×10^{-6} to 1×10^{-4}.

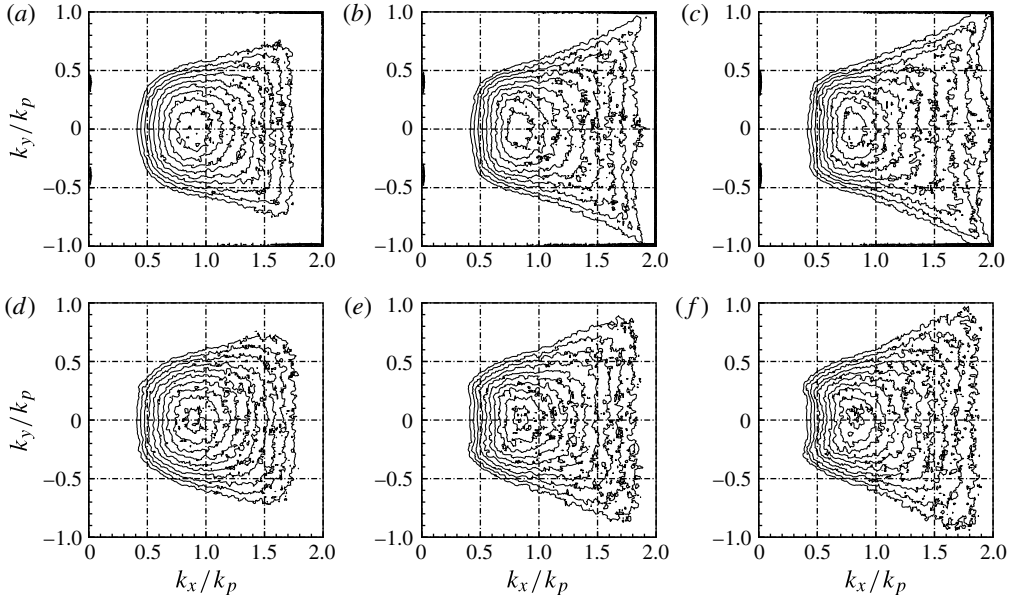

FIGURE 4. Evolution of the wavenumber spectrum $\Psi(\boldsymbol{k})$ of initially very narrow-band Gaussian spectrum (2.6) with $\varepsilon = 0.1$ and $\delta_k = 0.2$: (*a–c*) BMNLS; (*d–f*) HOS; (*a*,*d*) $t = 50T_p$; (*b*,*e*) $t = 100T_p$; (*c*,*f*) $t = 150T_p$. The contour values are logarithmic, ranging from 1×10^{-6} to 1×10^{-4}.

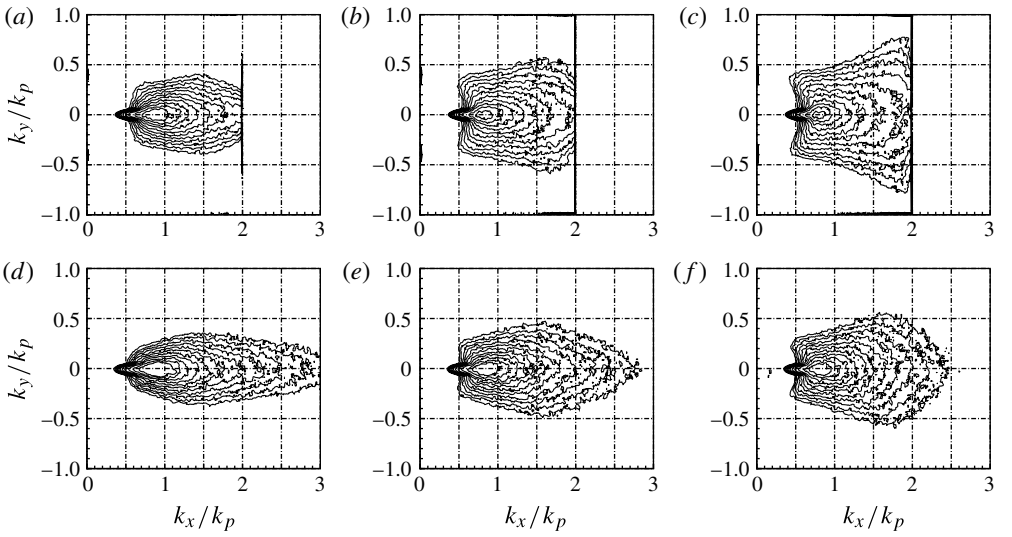

FIGURE 5. Evolution of the wavenumber spectrum $\Psi(\boldsymbol{k})$ of an initial JONSWAP spectrum with $H_s = 0.08$ m, $T_p = 1$ s, $\gamma = 6$ and $\Theta = 12°$: (*a–c*) BMNLS; (*d–f*) HOS; (*a*,*d*) $t = 50T_p$, (*b*,*e*) $t = 100T_p$, (*c*,*f*) $t = 150T_p$. The contour values are logarithmic, ranging from 1×10^{-6} to 1×10^{-4}.

Turning to the evolution of the (more realistic) JONSWAP spectrum, we are particularly interested in the effect of directional spreading on the spectral change. We consider initial spectra with the same steepness ε but different spreading angles Θ. These spectra have been used to generate random directional wave fields in the wave basin (Onorato *et al.* 2009). The spectral evolution of the wave field with small initial Θ is shown in figure 5. Again, the features of the spectral change are captured by both HOS and BMNLS, showing the significant directional broadening and spectral peak downshift. At large times $t \geqslant 100T_p$, and especially for shorter waves, BMNLS appears to overpredict the directional spreading. Similar results are observed in the case with large Θ (figure 6), although the spectral change is slower and less significant.

The spectral change is described more quantitatively through the omnidirectional spectrum and mean directional spread. The omnidirectional spectrum is defined as

$$S(k) = \int_\theta k\Psi(k,\theta)\,\mathrm{d}\theta, \tag{3.1}$$

where $k = |\boldsymbol{k}|$. The mean directional spread $\theta_m = \overline{\theta_2(k)}$ is defined as the average of the second-order moment of the directional distribution function $D(k,\theta)$ (Hwang *et al.* 2000; Toffoli *et al.* 2010):

$$\theta_2(k) = \left(\int_0^{\pi/2} \theta^2 D(k,\theta)\,\mathrm{d}\theta\right)^{1/2} \left(\int_0^{\pi/2} D(k,\theta)\,\mathrm{d}\theta\right)^{-1/2}. \tag{3.2}$$

Evolution of the omnidirectional spectra for the directional JONSWAP spectra is shown in figure 7. Both BMNLS and HOS predict the spectral peak downshift. The two models, however, differ qualitatively in the spectral tail. In the HOS predictions, the tail of $S(k)$ is nearly time-invariant and remains very close to the $k^{-2.5}$ power law for large k, for both narrow and broad spreading (figure 7*a*,*b*). This is not predicted by

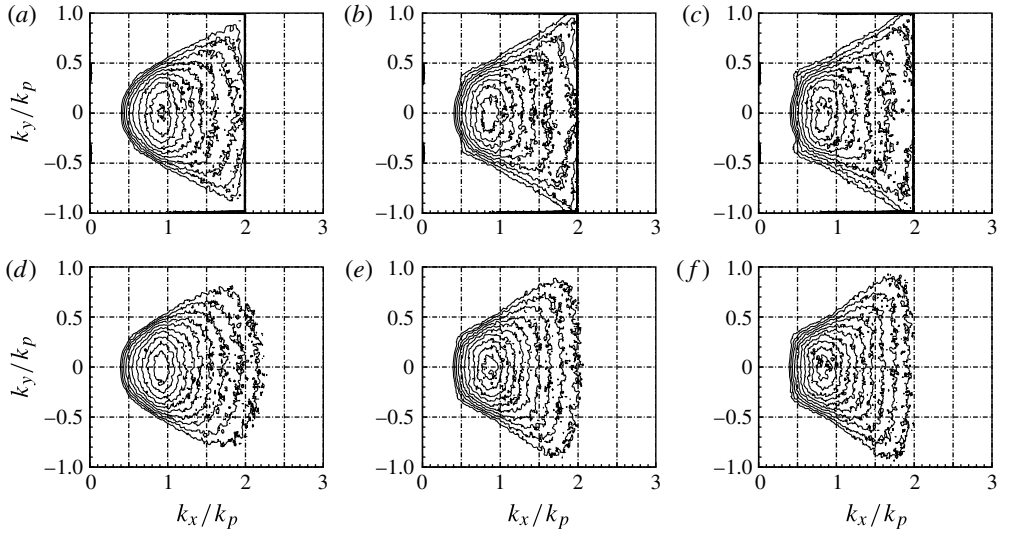

FIGURE 6. Evolution of the wavenumber spectrum $\Psi(\boldsymbol{k})$ of an initial JONSWAP spectrum with $H_s = 0.08$ m, $T_p = 1$ s, $\gamma = 6$ and $\Theta = 62°$: (*a–c*) BMNLS; (*d–f*) HOS; (*a*,*d*) $t = 50T_p$, (*b*,*e*) $t = 100T_p$, (*c*,*f*) $t = 150T_p$. The contour values are logarithmic, ranging from 1×10^{-6} to 1×10^{-4}.

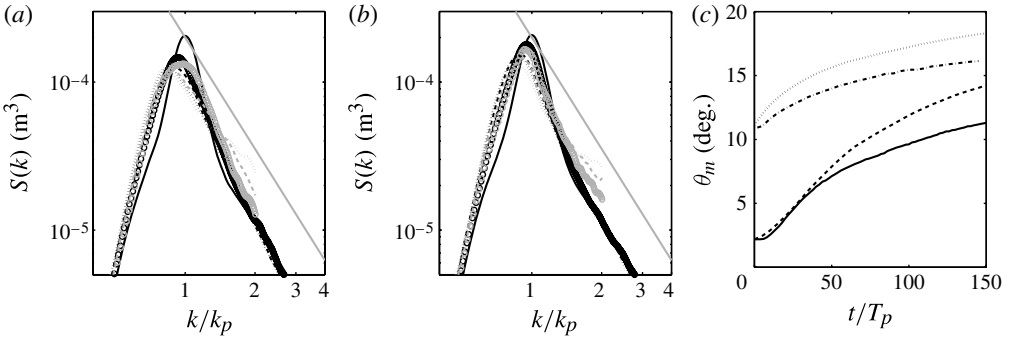

FIGURE 7. (*a*,*b*) Evolution of the omnidirectional spectrum of the wave fields with $H_s = 0.08$ m, $T_p = 1$ s and $\gamma = 6$ for (*a*) $\Theta = 12°$ and (*b*) $\Theta = 62°$. HOS: $t/T_p = 50$ (○), 100 (- - -), 150 (· · ·). BMNLS: $t/T_p = 50$ (○), 100 (– – –), 150 (· · ·); initial spectrum (—); $k^{-2.5}$ power law of spectral tail (—). (*c*) Temporal variation of mean directional spread θ_m. HOS: $\Theta = 12°$ (—), 62° (- · -). BMNLS: $\Theta = 12°$ (– – –), 62° (· · ·).

BMNLS, which shows continuous energy accumulation in time for short waves (owing to the absence of short-wave dissipation). Another measure of the spectral change is the evolution of the mean directional spread θ_m (figure 7*c*). For the initially narrow spread case, $\Theta = 12°$, HOS and BMNLS predict a similar increasing θ_m with evolution time up to $t/T_p \approx 50$. For large times, BMNLS overpredicts θ_m in comparison with HOS. For the initially broader spreading case, BMNLS overpredicts θ_m relative to HOS over the entire evolution. Comparing the two spreading cases, we see that the rate of change in θ_m is greater for smaller Θ as observed in figure 5. Note that

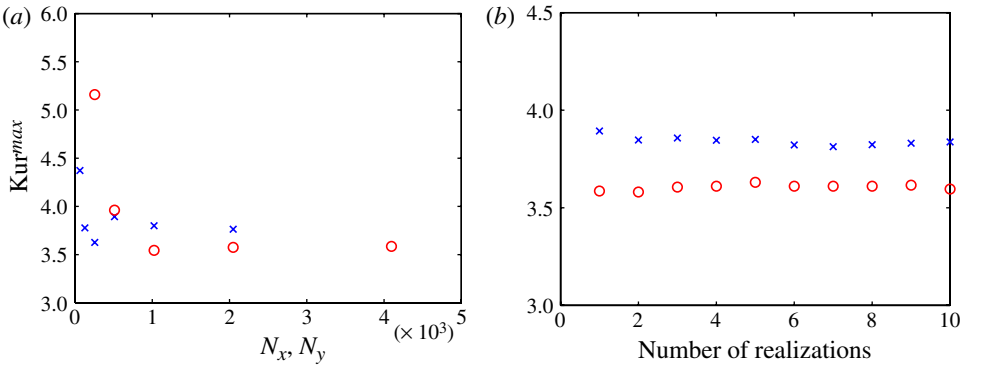

FIGURE 8. (Colour online) Convergence tests of maximum kurtosis by BMNLS (×) and HOS (○) as a function of (*a*) grid size and (*b*) number of realizations. The initial wave field is specified by a JONSWAP wave spectrum with $H_s = 0.08$ m, $T_p = 1$ s, $\gamma = 6$ and $\Theta = 12°$. For the results in panel (*b*), $N_x = N_y = 512$ and 4096 in BMNLS and HOS, respectively.

the difference between HOS and BMNLS predictions shown in these cases is related to directional spreading of the waves. For unidirectional waves, the difference in the predictions by the two models is generally smaller (Lo & Mei 1985; Stocker & Peregrine 1999; Shemer *et al.* 2002; Clamond *et al.* 2006; Shemer, Sergeeva & Slunyaev 2010*b*; Slunyaev & Sergeeva 2011).

3.2. *Statistics of nonlinear waves: direct comparisons to experiments*

We directly compare nonlinear statistics of directional random wave fields from HOS and BMNLS simulations with wave basin experiments (Onorato *et al.* 2009). The initial wave fields have identical steepness (ε) but a range of spectral bandwidths (γ) and spreading angles (Θ). To compare temporal BMNLS and HOS results with spatial records from experiments, a relation $x = c_g t$, where c_g is the group velocity of the peak wave, is used to convert from temporal variation to spatial variation. A discussion on the validity of this transformation can be found in Toffoli *et al.* (2010). In the computations, we use 4096×4096 grid points for the free surface in HOS and 512×512 grid points for the wave envelope in BMNLS. The wave statistics are obtained by ensemble averaging over five realizations. The values of these numerical parameters are chosen based on the convergence tests of the maximum kurtosis in the nonlinear evolution of a directional wave field, which are shown in figure 8.

3.2.1. *Exceedance probability of wave crests*

In HOS simulations the wave crests are defined as the local maxima of the wave surface, and in BMNLS simulations the wave crests are estimated as the third-order upper surface envelope $\eta_c = \overline{\eta} + |B_1| + |B_2| + |B_3|$. Figure 9 shows the exceedance probability of crests from experiments (Onorato *et al.* 2009) compared with BMNLS and HOS simulations, for wave fields with a range of spreading angles. Predictions from the Rayleigh distribution and second-order theory (Tayfun 1980) are also shown for reference. At location $x/\lambda_p\,(= t/2T_p) = 15.9$, where kurtosis reaches its maximum in the experiment, significant deviations of probability of large crests from both linear (Rayleigh) and second-order predictions are observed in both BMNLS and HOS, especially for small Θ. For initially broadly spreading seas, e.g. the $\Theta = 62°$ case, second-order theory provides a good prediction. In all cases, HOS appears to

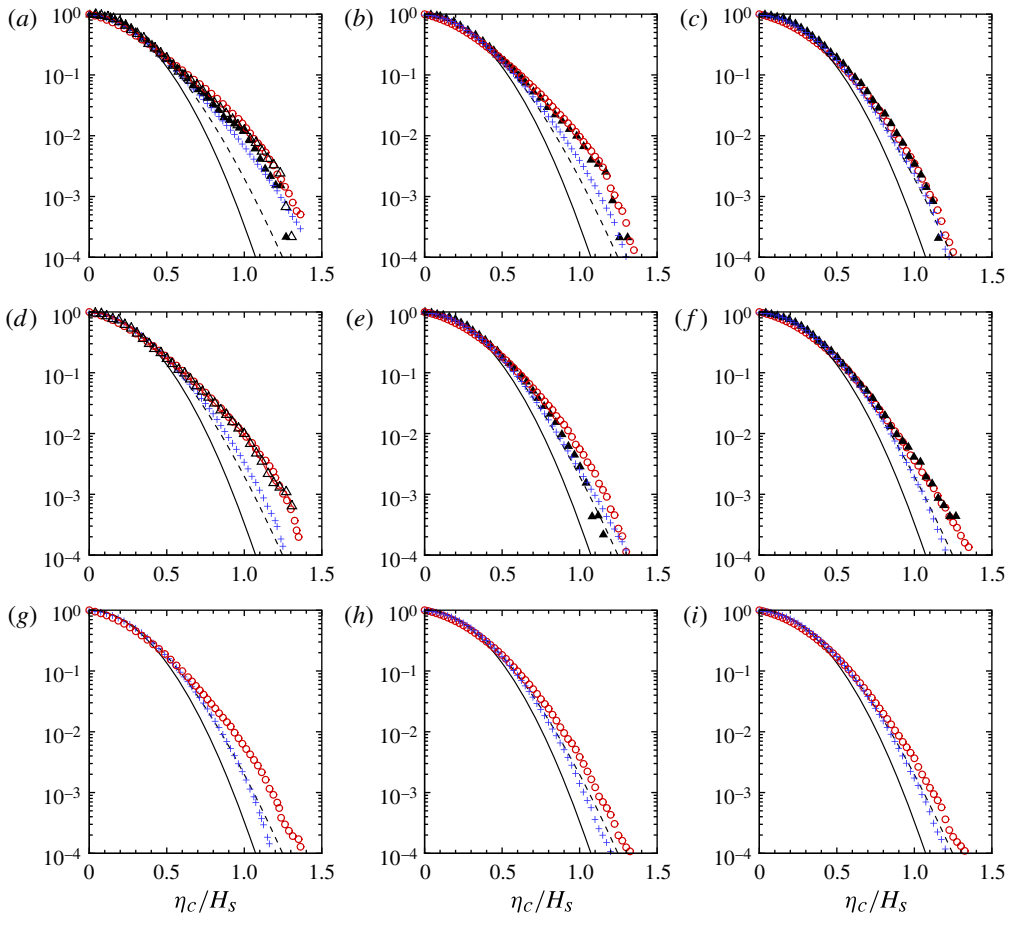

FIGURE 9. (Colour online) Exceedance probability of wave crests for JONSWAP wave fields with $H_s = 0.08$ m, $T_p = 1$ s, $\gamma = 6$ and three spreading angles: (*a*,*d*,*g*) $\Theta = 12°$, (*b*,*e*,*h*) 21° and (*c*,*f*,*i*) 62°, corresponding to exponents $s = 840$, 200 and 24 in the Mitsuyasu spreading function $\cos^s\theta$: (*a–c*) $x/\lambda_p = 15.9$, (*d–f*) $x/\lambda_p = 28.7$ and (*g–i*) $x/\lambda_p = 50$. Theory: HOS (○); BMNLS (+); Rayleigh distribution (——); second-order theory of Tayfun (1980) (– – –). Compared to experiment (Onorato *et al.* 2008, 2009) for: unidirectional (△) and $s = 840$, 200, 24 (▲). (Experimental values for $\Theta = 12°$ at $x/\lambda_p = 28.7$ are not published.) HOS and BMNLS results are averaged over five realizations.

achieve a better overall comparison to measured values. At $x/\lambda_p\,(= t/2T_p) = 28.7$, the farthest location from the wavemaker in the experiment, the exceedance probability (somewhat reduced now relative to $x/\lambda_p = 15.9$) remains significantly different from linear and second-order theory, especially for $\Theta = 12$ and 62°. HOS agrees very well with measurements, while BMNLS predictions tend towards those from second-order theory. For useful rogue wave predictions, our interest is in even longer evolution times, in particular after wave-field statistics have reached quasi-steady state ($t/T_p = 2x/\lambda_p \gtrsim O(100)$) predicted by HOS (see § 3.2.2). Figure 9(*g–i*) shows the results for $t/2T_p = x/\lambda_p = 50$. In this case, BMNLS predictions remain close to second-order theory, while HOS predicts considerably higher probability of large crests for all Θ and especially for small initial spreading angles.

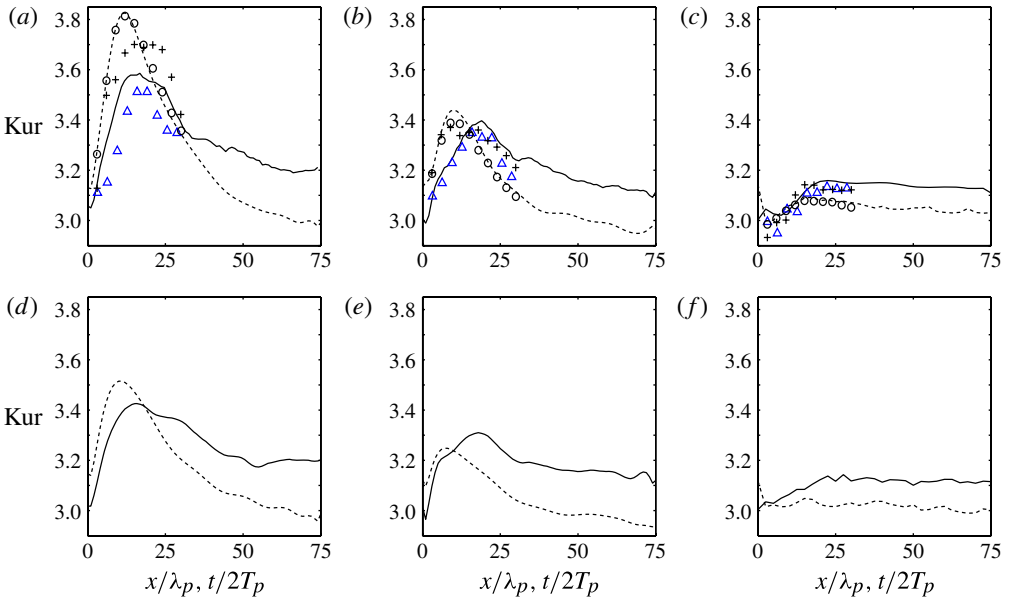

FIGURE 10. (Colour online) Spatial variation of kurtosis for JONSWAP directional wave fields with $H_s = 0.08$ m, $T_p = 1$ s ($\varepsilon = 0.16$), $\gamma = 6$ (*a–c*) and 3 (*d–f*), and spreading angles $\Theta = 12°$ (*a*,*d*), 21° (*b*,*e*) and 62° (*c*,*f*). Experiment (Onorato *et al.* 2009): △(experimental results for $\varepsilon = 0.16$, $\gamma = 3$ are not available). Theory: HOS (——), BMNLS (– – –). HOS and BMNLS results are averaged over five realizations. The results from Toffoli *et al.* (2010) are also shown: BMNLS (◯) and HOS (+).

3.2.2. *Kurtosis of surface elevation*

Kurtosis of the wave elevation, defined as $\text{Kur} \equiv \langle \eta^4 \rangle / \langle \eta^2 \rangle^2$, is found to be an important indicator for rogue wave occurrence (Mori & Janssen 2006). Figure 10 shows comparisons of the evolution of kurtosis for wave fields with a range of γ and Θ, obtained from experiments (Onorato *et al.* 2009), HOS and BMNLS simulations. In BMNLS simulations, kurtosis is calculated based on the third-order reconstruction of surface elevation (2.3). Similar results have been obtained in Toffoli *et al.* (2010), and their results are included in figure 10 for comparison. Our BMNLS results agree completely with those of Toffoli *et al.* (2010). For the HOS results, there is a noticeable difference between the present prediction and that of Toffoli *et al.* (2010). This is due to the lower HOS resolutions used in Toffoli *et al.* (2010) (corresponding to $N_x, N_y = 256$ in figure 8*a*). For both BMNLS and HOS, for wave fields with small spreading angles, we find that kurtosis increases from initial value of Kur ≈ 3, coinciding with the initial rapid spectral broadening observed in figure 5 due to MI. BMNLS overestimates kurtosis during this time. At large times, in BMNLS simulations, kurtosis reduces to the Gaussian value or below. This continuous decrease of kurtosis in BMNLS at long times is also observed in the model simulations of Socquet-Juglard *et al.* (2005). From our BMNLS simulations, we find that the continuous decrease of kurtosis results from the fact that, in the large-time evolution, the contribution to kurtosis from free waves continues to decrease while that from bound waves remains almost unchanged. This is probably due to the incomplete accounting for quartet wave interactions in BMNLS (see e.g. Janssen 2003).

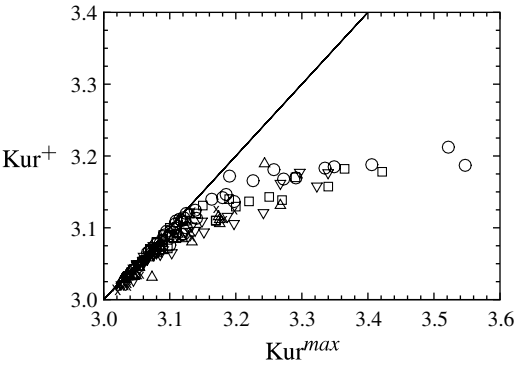

FIGURE 11. Kur^{max} versus Kur^{+} for ∼200 wave fields with a range of spectral parameters ε, γ and Θ from MIT-Wave: $\varepsilon = 0.06$ (×); 0.08 (△); 0.1 (▽); 0.12 (□); 0.14 (◯).

In HOS simulations, kurtosis decreases slowly to a quasi-stationary value, which is nearly invariant over time $100 \leqslant t/T_p\,(= 2x/\lambda_p) \leqslant 150$ (and beyond). The quasi-stationary kurtosis obtained from HOS is considerably non-Gaussian. There is some evidence to suggest that the value of kurtosis may eventually become Gaussian at long time evolution (see Annenkov & Shrira 2009*a*). For wave fields with large spreading angles (e.g. $\Theta = 62°$), both BMNLS and HOS predict slower variations of kurtosis over time, consistent with the slower spectral change observed in figure 6. Overall, HOS consistently obtains greater values of kurtosis for longer times. HOS also appears to achieve better comparisons to measurements over the different wave fields considered.

For later reference, we define the maximum value, $(\,)^{max}$, say, of kurtosis, attained during the entire HOS simulation (up to $t/T_p = 150$), as well as the average value, $(\,)^{+}$, obtained over the quasi-steady phase of the HOS evolution ($100 \leqslant t/T_p \leqslant 150$). The values of Kur^{max} and Kur^{+} can be readily observed graphically from figure 10. The deviation of Kur^{max} from the Gaussian statistics ($\mathrm{Kur} = 3$) becomes more significant as the initial Θ decreases. For given Θ, Kur^{max} is greater in wave fields with narrower spectral bandwidth (larger γ). In BMNLS simulations, Kur^{max} is significantly overpredicted for small Θ, and generally obtained at an earlier time relative to experiments and HOS predictions. This is also observed in Toffoli *et al.* (2010). Note that the evolution of kurtosis in HOS simulations is found to be insensitive to the initial period of $\sim 5T_p$ over which the nonlinear terms in the free-surface boundary conditions are smoothly ramped up.

Aggregating $O(200)$ HOS simulations in the MIT-Wave database for a broad range of initial spectral parameters, figure 11 plots the predicted values of $(\mathrm{Kur}^{max}, \mathrm{Kur}^{+})$ for these cases. We see a clear relationship between Kur^{+} and Kur^{max}. For smaller Kur^{max} ($\leqslant \mathrm{Kur}^{a} \approx 3.2$), $\mathrm{Kur}^{+} \approx \mathrm{Kur}^{max}$; while for greater Kur^{max}, Kur^{+} remains almost constant (≈3.2) with increasing values of Kur^{max}. These suggest that, for evolutions with $\mathrm{Kur}^{max} \lesssim \mathrm{Kur}^{a}$, Kur^{max} is reached in the asymptotic quasi-steady state; while for evolutions with $\mathrm{Kur}^{max} \gtrsim \mathrm{Kur}^{a}$, Kur^{max} is reached at an early phase of the evolution, which then decreases towards the longer-time average value Kur^{+}. The latter case is indicative of significant MI resulting in rapid change of the (initial) spectra and strongly nonlinear/non-Gaussian wave statistics, while the former case corresponds to the absence of significant MI, resulting in a slowly varying wave field and slowly developing non-Gaussian statistics. An estimation of kurtosis using second-order theory gives $\mathrm{Kur}_2 = 3 + 24\,(k_p\sigma)^2$ (Longuet-Higgins 1963; Onorato *et al.* 2009).

For the wave fields in figure 11, the largest (initial) steepness is $\varepsilon = 0.14$, which gives $\mathrm{Kur}_2 = 3.12$. This value is considerably smaller than Kur^a. This underestimation of kurtosis by Kur_2 is related to the narrow-band assumption in the derivation of Kur_2, as discussed in Janssen (2009).

4. Probability of rogue wave occurrence

We investigate the occurrence probability of rogue waves and its dependence on (initial) wave spectral parameters. To do this, we use the HOS model to simulate a large number ($O(200)$) of nonlinear three-dimensional ocean wave fields (the MIT-Wave dataset) with initial JONSWAP spectra covering a broad range of spectral steepness $\varepsilon = H_s k_p/2$, frequency bandwidths (controlled by the peakedness enhancement factor γ), and spreading angles Θ. In the MIT-Wave dataset, ε ranges from 0.06 to 0.14 with increment 0.2, γ varies over 1, 3.3, 5, 6 and 10, and $\Theta = 20,\ 30,\ 40,\ 60,\ 80,\ 100$ and 120°. For unidirectional wave fields, a measure of the importance of MI is $\mathrm{BFI} \equiv \varepsilon/(\Delta k/k_p) > 1/\sqrt{2}$ (Janssen 2003). The corresponding value of BFI for the MIT-Wave dataset ranges from 0.1 to 1.1 (the spectral bandwidth Δk is calculated as the half-width at half-maximum of the wavenumber spectrum).

4.1. *Identification of rogue waves*

For the purpose of identifying a large *rogue wave* (group), we use the criterion that the crest-to-trough wave height H exceeds $H/H_s \geqslant \alpha$. In this study, we use $\alpha = 2.0$. In the context of long-crested waves, the identification of a wave (or wave group), and hence its crest-to-trough height, is obtained readily in terms of, say, zero crossings. For short-crested seas, this is problematic. Nevertheless, for the identification of rogue waves, large wave events are generally isolated from the ambient small waves, which allows us to obtain a meaningful identification and definition.

The precise definition of the extent of the rogue wave event (within which $H \geqslant \alpha H_s$ holds) is not unique, however, the final results and conclusions are not very sensitive to the specific procedure used (Xiao 2013). For the present study, we use the following procedure (the results below are unaffected if 'crest' and 'trough' are interchanged). At any given time, for every local maxima ('crest') located at, say, $\boldsymbol{x}_c = (x_c, y_c)$, in the wave field, we define a rectangular region $\mathscr{R}$ centred on $\boldsymbol{x}_c$, given by $|x - x_c| \leqslant \lambda_p$ and $|y - y_c| \leqslant C_y$, where $C_y = \lambda_y/2$ is the average crest length and λ_y is the average wavelength in the y direction (defined in (4.2)). Within each $\mathscr{R}$ we search for all the minima ('trough') points to evaluate the corresponding H. If the maximum H thus obtained satisfies $H/H_s \geqslant \alpha$, a rogue wave is identified associated with the corresponding crest–trough pair $\boldsymbol{x}_c$ and $\boldsymbol{x}_t$. In the case where an $\boldsymbol{x}_t$ is shared by two or more $\boldsymbol{x}_c$ (centred on different $\mathscr{R}$), only the $\boldsymbol{x}_c, \boldsymbol{x}_t$ pair that obtains the maximum H among these (and the corresponding $\mathscr{R}$) is counted. Note that, in the above procedure, the result is invariant if crest and trough are interchanged. This is in contrast to identification of rogue waves based on one-dimensional time series of wave elevation, where the number of rogue waves is different depending on the use of zero up- or down-crossing (Guedes Soares, Cherneva & Antão 2003; Pinho, Liu & Ribeira 2004).

4.2. *Number probability of rogue waves*

The number probability of rogue waves at a given time, denoted as P_N, can be defined as

$$P_N = N_{rogue}/N_w, \tag{4.1}$$

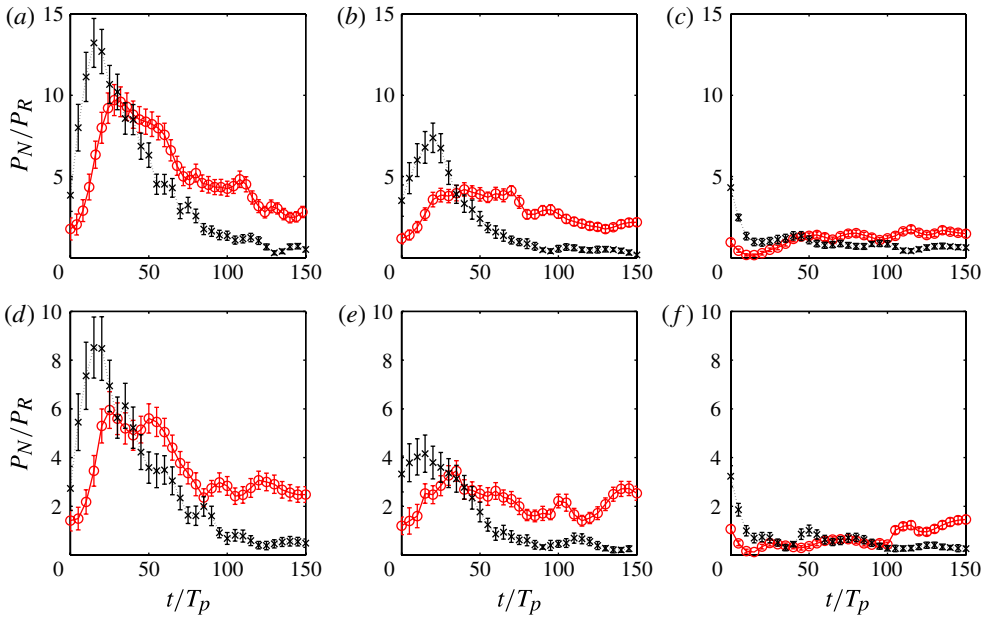

FIGURE 12. (Colour online) Evolution of the number probability of rogue waves P_N for JONSWAP wave fields $H_s = 0.08$ m, $T_p = 1$ s, $\gamma = 6$ (*a–c*) and 3 (*d–f*), and spreading angles $\Theta = 12°$ (*a*,*d*), 21° (*b*,*e*) and 62° (*c*,*f*). HOS (○); BMNLS (×). The standard deviations of the statistic, $\pm P_N/\sqrt{N_{rogue}}$, are indicated as error bars. Results are scaled by the Rayleigh distribution $P_R = 3.35 \times 10^{-4}$ for $H/H_s \geqslant \alpha$, $\alpha = 2$. HOS and BMNLS results are averaged over five realizations.

where N_{rogue} is the number of rogue waves identified, and N_w the total number of waves in the wave field. For a general short-crested wave field, the precise value of N_w can be difficult to obtain (or define). For specificity, we set $N_w = L_x L_y/\bar{a}$, where $\bar{a}$ is the average area of a wave, estimated by Piterbarg (1996) and Socquet-Juglard *et al.* (2005) as

$$\bar{a} = \lambda_x \lambda_y/\sqrt{2\pi} \quad \text{and} \quad \lambda_{x,y} = 2\pi/\langle k_{x,y}^2 \rangle^{1/2}, \quad \langle k_{x,y}^2 \rangle = \int k_{x,y}^2 \Psi(\boldsymbol{k})\,\mathrm{d}\boldsymbol{k} \Big/ \int \Psi(\boldsymbol{k})\,\mathrm{d}\boldsymbol{k}. \quad (4.2)$$

Note that, with this definition, N_w varies in time as the spectrum changes, and generally increases with directional spreading.

Figure 12 shows the evolution of P_N from HOS and BMNLS simulations. The convergence of the P_N statistic, estimated by the standard deviation $P_N/\sqrt{N_{rogue}}$, is indicated as error bars. For small (initial) spreading angles (figure 12*a*,*d*), from both BMNLS and HOS simulations, P_N increases initially over a time scale corresponding to the rapid spectral change (see figure 5), reaching values of P_N^{max} that are an order of magnitude greater than the linear prediction. During this time, BMNLS overestimates P_N. At larger times, P_N decreases, with BMNLS predictions approaching the Rayleigh prediction P_R, where, for HOS, P_N approaches a quasi-stationary non-Gaussian value, which is many times greater than P_R and the BMNLS predictions. Contrasting figures 12(*a*) and 12(*d*), it is clear that the magnitude of P_N is greater for narrower (initial) frequency bandwidth (larger γ) corresponding to stronger MI.

For greater spreading angles, the qualitative trends remain, although the amplification of P_N relative to P_R is progressively less significant. For the very broadly spreading case $\Theta = 62°$, P_N in HOS generally increases slowly with time (towards the quasi-stationary value); while in BMNLS, P_N monotonically decreases with time, eventually becomes smaller than P_R.

In summary, we see that P_N generally increases with decreasing Θ and increasing γ, with P_N^{max} many times greater than P_R for narrow spreading wave fields, and generally reached over a relatively small time scale corresponding to the initial strong MI of the wave field. In all cases, HOS obtains a nonlinear quasi-static state after a long time, with P_N^+ still many times greater than P_R (and BMNLS predictions).

Comparing figures 12 and 10 corresponding to the same (initial) spectral parameters, the qualitative resemblance between P_N and kurtosis is quite apparent, suggesting that the latter is a good indicator/predictor of the likelihood of rogue waves. To better understand the quasi-stationary probability of rogue waves at large time predicted by HOS, we plot P_N^+ versus P_N^{max} for ∼200 wave fields in the MIT-Wave dataset (figure 13). Similar to figure 11, the ensemble of wave cases fall into two relatively distinct categories. For cases with relatively small P_N^{max} ($\lesssim 4P_R$), $P_N^+ \approx P_N^{max}$, indicating that P_N^{max} is obtained in the quasi-stationary state. For greater P_N^{max}, P_N^+ shows some scatter but is aggregated around $P_N^+/P_R \sim 4$. These latter cases correspond to situations where P_N^{max} is achieved due to strong initial MI before the quasi-stationary state.

4.3. *Area probability of rogue waves*

As we pointed out earlier, the number probability of rogue waves in terms of relative frequency of *number* of (rogue) waves is problematic for (very) broad directional spreading waves. For short-crested seas, N_{rogue} does not distinguish between events of different sizes, while the validity of (4.2) for estimating the total number of waves N_w may be questioned. The problem is exacerbated by the fact that even initially narrow spreading spectra tend to evolve towards broader spreading (see e.g. figure 7*c*); and furthermore, as the spectrum evolves, N_w is a time-varying (but *a priori* unknown) function (for instance, for the case of figure 12*a*, N_w at $t = 150T_p$ is over four times its initial value).

To overcome these problems, we introduce a general and robust area probability of rogue waves, denoted by P_A, as a useful measure of the likelihood of rogue waves for general directional spread wave fields. This probability P_A is defined as

$$P_A = A_{rogue}/A_w, \tag{4.3}$$

where A_{rogue} is the total area of rogue waves, and $A_w = L_x L_y$ is the total area of the wave field under consideration (which, unlike N_w, is invariant). After a rogue wave event is identified (see § 4.1), its area a_{rogue} is defined as the sum of the zero elevation contours enclosing the crest point $\boldsymbol{x}_c$ and trough point $\boldsymbol{x}_t$ associated with the rogue wave. Clearly P_A is applicable for any general directional spread sea.

Note that, while both $P_N, P_A \in [0, 1]$ are well defined as probabilities, their quantitative values can differ substantially for short-crested wave fields. In general, P_A and P_N are related by

$$P_A/P_N = \bar{a}_{rogue}/\bar{a}, \tag{4.4}$$

where $\bar{a}_{rogue} = A_{rogue}/N_{rogue}$ is the average area of a rogue wave. For unidirectional seas, $P_A \approx P_N$ for very narrow-band wave fields; while for broad(er) band waves, P_A and P_N are expected to be of comparable magnitudes. In § 5.1.1, we find $\lambda_{rogue} \approx \lambda_p$, so that $P_A/P_N = \bar{\lambda}_{rogue}/\lambda_x \gtrsim 1$ (since $\lambda_p > \lambda_x$ for the JONSWAP spectrum). For short-crested

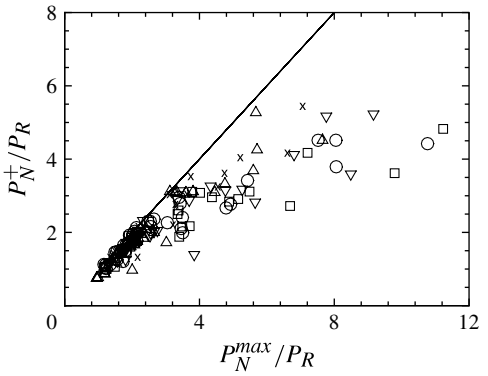

FIGURE 13. Plot of P_N^{max} versus P_N^+ for ∼200 wave fields with a range of ε, γ and Θ from MIT-Wave: $\varepsilon = 0.06$ (×); 0.08 (△); 0.1 (▽); 0.12 (□); 0.14 (◯).

wave fields, the value of $\bar{a}_{rogue}/\bar{a}$ is not generally known. In § 5.1.2, we find that $\bar{a}_{rogue}/\bar{a} \approx O(5)$ (depending on wave-field parameters, see figure 22).

Figure 14 shows the evolution of P_A for the same cases considered in § 4.2. Comparing figures 14 and 12, we observe that the qualitative trends of P_N and P_A are somewhat similar, except that the magnitude of P_A is several times (∼5) greater than P_N, indicative of $\bar{a}_{rogue}$ much greater than $\bar{a}$, characteristic of short-crested seas. The notable difference between P_A and P_N is seen in the initially narrow spread cases ($\Theta = 12$ and 21°), where BMNLS now consistently underestimates P_A throughout the evolutions. As observed earlier, P_A predicted by HOS again displays the quasi-stationary state after $t/T_P \gtrsim O(100)$; while the BMNLS-predicted P_A diminishes monotonically with increasing time.

Figure 15 shows the relation between P_A^+ and P_A^{max} for the ∼200 wave fields that we used in the MIT-Wave dataset. We observe a very similar pattern relative to those for kurtosis and P_N (figures 11 and 13). In this case, the threshold value beyond which P_A^+ departs from P_A^{max}, and MI is significant in the (initial) evolution, is $P_A^+/P_R \approx 20$. With the more valid definition of rogue wave occurrence in terms of area, the scatter in $P_A^+/P_R \approx 20$ obtained in the quasi-stationary state is substantially reduced. Despite the range of P_N^{max}/P_R spanning over an order of magnitude, the quasi-stationary value of $P_A^+/P_R \approx 20$ has a remarkably narrow range, suggesting that this might be a somewhat (more) common value of probability of occurrence of rogue waves ($H/H_s \geqslant \alpha = 2$) under a broad range of ocean wave-field conditions for which MI is relevant. For greater (smaller) values α, this threshold (quasi-stationary) value of P_A^+/P_R is expected to increase (decrease), which we verify (details are not presented; see Xiao (2013)).

4.4. *Dependence of rogue wave probability on kurtosis, and on BFI*

The probability of rogue wave occurrence has been found to be closely related to the kurtosis of the wave field at a given time. Figure 16 plots P_N^{max} and P_A^{max} as functions of Kur^{max} for the ∼200 wave fields from the MIT-Wave dataset. For comparison, we also include the MER distribution for the 'number' exceedance probability of wave heights, wherein the third-order wave nonlinearity effects related to MI are included (Mori & Yasuda 2002; Mori & Janssen 2006).

We see that both P_N^{max} and P_A^{max} have almost linear correlations with Kur^{max} for the full range of Kur^{max} that we obtained from broad ranges of (initial) spectral parameters

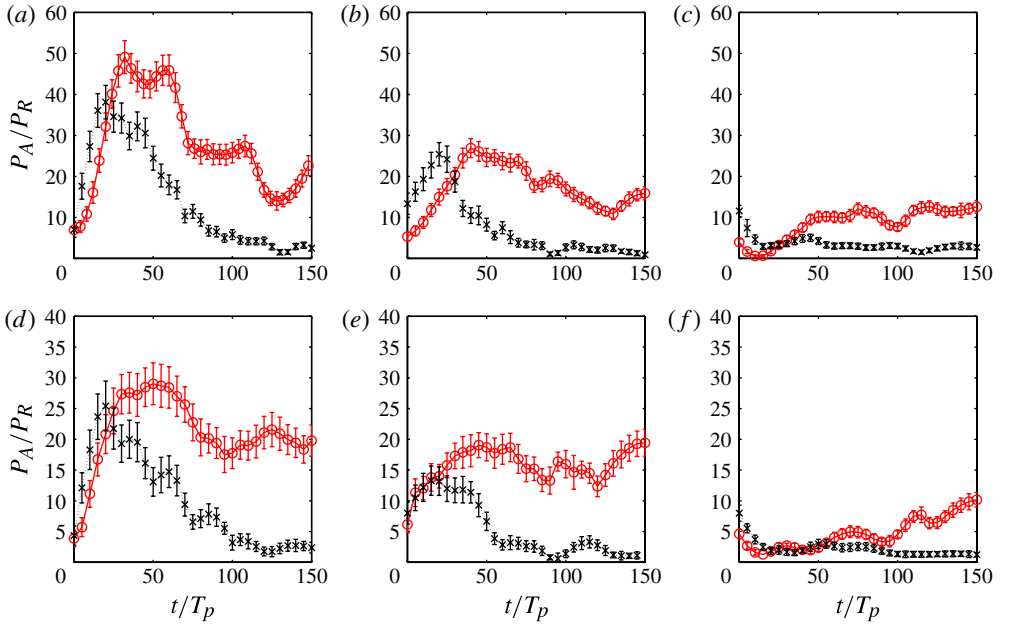

FIGURE 14. (Colour online) Evolution of the area probability of rogue waves P_A for JONSWAP wave fields $H_s = 0.08$ m, $T_p = 1$ s, $\gamma = 6$ (*a–c*) and 3 (*d–f*), and spreading angles $\Theta = 12°$ (*a*,*d*), 21° (*b*,*e*) and 62° (*c*,*f*). HOS (○); BMNLS (×). The standard deviations of the statistic, $\pm P_A/\sqrt{N_{rogue}}$, are indicated as error bars. Results are scaled by the Rayleigh distribution $P_R = 3.35 \times 10^{-4}$ for $H/H_s \geqslant \alpha$, $\alpha = 2$. HOS and BMNLS results are averaged over five realizations.

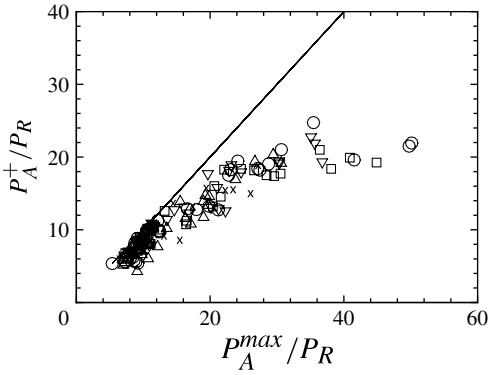

FIGURE 15. Plot of P_A^{max} versus P_A^+ for ∼200 wave fields with a range of ε, γ and Θ from MIT-Wave: $\varepsilon = 0.06$ (×); 0.08 (△); 0.1 (▽); 0.12 (□); 0.14 (◯).

in the MIT-Wave cases considered. For P_N^{max}, MER substantially underestimates the occurrence probability and appears to be relevant only for small Kur values (above Kur = 3). Comparing figures 16(*a*) and 16(*b*), it is evident that P_A^{max} has a better linear correlation (with higher R^2 value) relative to P_N^{max} (especially for greater Kur^{max}). This is not surprising, since many of the MIT-Wave wave fields are (eventually) broadly spread. Clearly, P_A is a preferred measure of rogue wave probability for general wave-field conditions.

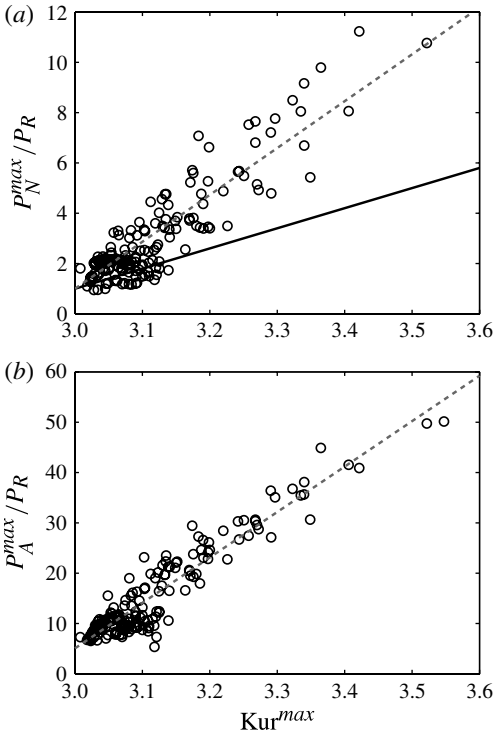

FIGURE 16. Plots of (*a*) P_N^{max} versus Kur^{max} and (*b*) P_A^{max} versus Kur^{max} for ∼200 directional wave fields from MIT-Wave. HOS (◯); MER (Mori & Janssen 2006) (——). Linear regression lines (- - -): $P_N^{max}/P_R = 1 + 18.64(\text{Kur}^{max} - 3)$ (coefficient of determination $R^2 = 0.82$); $P_A^{max}/P_R = 5.06 + 90.30(\text{Kur}^{max} - 3)$ ($R^2 = 0.89$).

The dependence of kurtosis on BFI has been investigated theoretically, numerically and experimentally. For unidirectional wave fields with very narrow-band Gaussian spectra, Mori & Janssen (2006) show that $\text{Kur} = 3 + 2\pi\,\text{BFI}^2/\sqrt{3}$, where $\text{BFI} = \varepsilon/(\Delta k/k_p)$ ($\varepsilon = k_p H_s/2$). The direct dependence of Kur on BFI for unidirectional seas with more general spectra has also been observed in wave flume experiments (Onorato *et al.* 2004). For short-crested wave fields, however, it is found from experiments and NLS-type simulations that the dependence of kurtosis on BFI is greatly reduced (Gramstad & Trulsen 2007; Onorato *et al.* 2009; Waseda *et al.* 2009).

Figure 17 plots Kur^{max} versus (initial) BFI-squared for MIT-Wave wave fields varying over a range of Θ (and ε and γ). The effect of direction spreading on the correlation between Kur and BFI-squared is clearly seen, especially for large BFI. For the very narrow spreading cases, Kur^{max} has a clear linear correlation with BFI^2, especially for Kur$^{max} \geqslant 3.2$. For large Θ, a linear (trend) correlation between Kur^{max} and BFI^2 is still seen; however, the slope with which Kur^{max} depends on BFI^2 decreases with increasing Θ, so that, for very broad spread cases, Kur^{max} is almost independent of BFI, although, for a given Θ, we observe linear-like correlation between kurtosis and BFI^2. For given BFI, the value of kurtosis is still unknown if the influence of spreading angle is not considered. Using just BFI without Θ information creates huge scatter because of different rate of dependences on BFI.

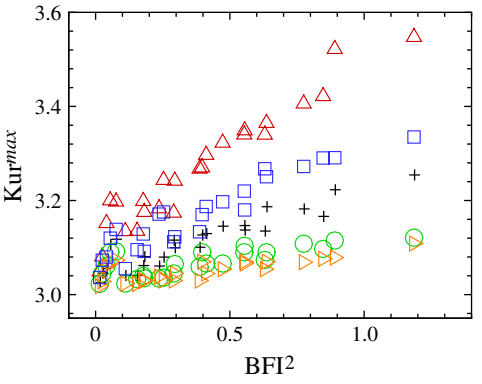

FIGURE 17. (Colour online) Dependence of Kur^{max} on the initial BFI^2 for wave fields with a range of ε, γ and Θ in MIT-Wave: $\Theta = 20°$ (△); 30° (□); 40° (+); 80° (○); 120° (▷).

4.5. *MBFI for predicting rogue wave occurrence*

The above findings suggest the need for a more general MI spectral parameter, applicable to wave fields with arbitrary directional spreading, that measures the probability of extreme waves. Different forms of modified BFI have been proposed by Waseda *et al.* (2009) and Mori *et al.* (2011). The parametrization in Waseda *et al.* (2009), which is obtained based on a limited number of wave basin experiments, does not reflect the general feature of monotonic reduction of kurtosis with increasing spreading angle. The modified BFI in Mori *et al.* (2011) is obtained by numerical fitting to the results from NLS simulations.

We introduce a modified Benjamin–Feir index (MBFI) defined as

$$\mathrm{MBFI} = \left[\frac{1+\tan^2(\Theta/2)}{1+4\tan^2(\Theta/2)}\right]\frac{\varepsilon}{\Delta k/k_p}, \tag{4.5}$$

i.e. $\mathrm{MBFI} = F(\Theta)\mathrm{BFI}$, where $F(\Theta)$ is the quantity in the square brackets in (4.5). For unidirectional wave fields $F(0) = 1$ and $\mathrm{MBFI} = \mathrm{BFI}$; while for very broadly directional spread seas, $\mathrm{MBFI}/\mathrm{BFI} = F(180°) = 0.25$.

This definition of MBFI (4.5) is derived based on a generalization of the result of Alber (1978), who considered the effect of three-dimensional disturbance on the stability of the very narrow-band Gaussian spectrum (2.6). In this case, the wave field is unstable for

$$\frac{2\sqrt{2}k_p\sigma}{\Delta k/k_p}G(K_x, K_y) > 1, \quad G(K_x, K_y) = \left[\frac{1-2\,(K_y/K_x)^2}{1+(2K_y/K_x)^2}\right]^{1/2}, \tag{4.6}$$

where K_x and K_y are the modulation wavenumbers in the x and y directions, and Δk is the spectral bandwidth in the x direction. The effect of the presence of transverse disturbance $G(K_x, K_y)$ can be related to the directional spreading Θ by taking, say, $\Theta = 2\tan^{-1}(K_y/K_x)$ and writing

$$G(K_x, K_y) = \left[\frac{1-2\,(K_y/K_x)^2}{1+(2K_y/K_x)^2}\right]^{1/2} \simeq \left[\frac{1-2\tan^2(\Theta/2)}{1+4\tan^2(\Theta/2)}\right]^{1/2}$$
$$\approx \frac{1+\tan^2(\Theta/2)}{1+4\tan^2(\Theta/2)} \equiv F(\Theta), \tag{4.7}$$

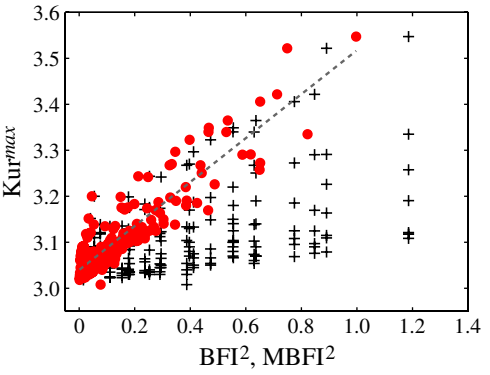

FIGURE 18. (Colour online) Dependence of Kur^{max} on BFI^2 and MBFI^2 for ∼200 wave fields from MIT-Wave: BFI (+); MBFI (●). Linear regression line (- - -): $\mathrm{Kur}^{max} = 0.48\mathrm{MBFI}^2 + 3.04$ ($R^2 = 0.82$).

where the last approximation, valid for small Θ, is used to make $F(\Theta)$ defined for general values of $\Theta \in [0, 180°]$.

Figure 18 shows the dependence of Kur^{max} on MBFI and BFI for the MIT-Wave data. With MBFI, the scatter in the data is greatly reduced, resulting in a clear and almost linear parametrization of Kur^{max} and MBFI^2 over the broad range of initial spectral parameters that we considered, especially in the range $\mathrm{Kur}^{max} \gtrsim 3.2$. This indicates that $F(\Theta)$ (4.7) is a reasonable description of the influence of the spreading angle on the maximum value of kurtosis.

Given the known dependence of rogue wave occurrence on kurtosis, it is expected that MBFI would also be the (single) metric for the occurrence probability. This is shown in figure 19, where we see a remarkable correlation between occurrence probability and MBFI especially for P_A. Indeed, a linear fit holds:

$$P_A/P_R \approx b_1 \times \mathrm{MBFI}^2 + b_0, \tag{4.8}$$

where, over a broad range of spectral parameters, b_0 and b_1 are functions of the rogue wave criterion $H/H_s \geqslant \alpha$ only. For figure 19, $\alpha = 2$, and we obtain $b_0 = 8.60$ and $b_1 = 43.88$ with $R^2 = 0.76$. A similar fit obtains for P_N/P_R with a somewhat smaller $R^2 = 0.67$. Considering the broad range of wave-field conditions represented in figure 19, the surprisingly simple result (4.8) is noteworthy.

Figure 20 shows the (colour) contours of the number and area probabilities of rogue wave occurrence, as functions of $F^2(\Theta)$ and BFI^2, compiled from the $O(200)$ large-scale simulations in MIT-Wave. Also included in the figure are the hyperbolic contour lines corresponding to $\mathrm{MBFI}^2 = \mathrm{BFI}^2\, F^2(\Theta) = \text{constant}$. We see a strong dependence on Θ, suggesting that prediction of the occurrence using BFI alone is inadequate (except for the special case of very small Θ, i.e. large $F(\Theta)$). The general dependence on both BFI and Θ is generally captured by MBFI, with the suggested fit (4.8) clearly shown in the comparison between the computed probabilities and the MBFI^2 contours. Comparing P_N/P_R and P_A/P_R, it appears that P_A/P_R is better parametrized by MBFI, especially for greater values of directional spreading Θ (smaller values of $F(\Theta)$ and MBFI), as expected.

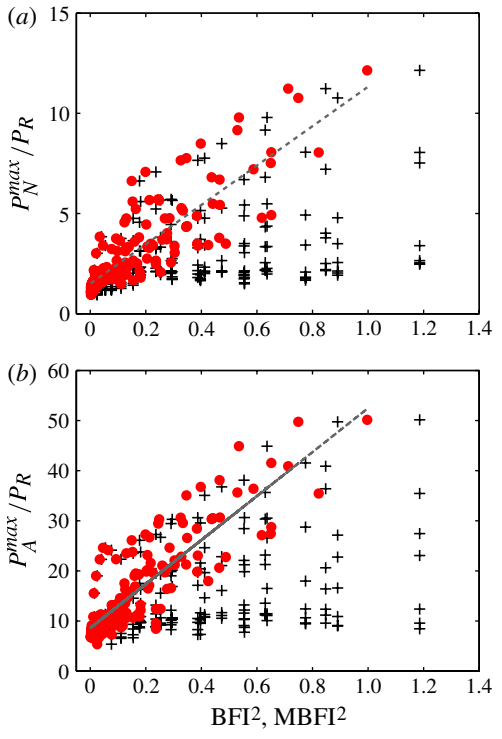

FIGURE 19. (Colour online) Dependence of (*a*) P_N^{max}/P_R and (*b*) P_A^{max}/P_R on BFI^2 and MBFI^2 for ∼200 wave fields from MIT-Wave for $\alpha = 2$: BFI (+); MBFI (●). Linear regression line (- - -), equation (4.8) with $b_0 = 8.60$, $b_1 = 43.88$ ($R^2 = 0.76$) for P_A/P_R; and $b_0 = 1.51$, $b_1 = 9.80$ ($R^2 = 0.67$) for P_N/P_R.

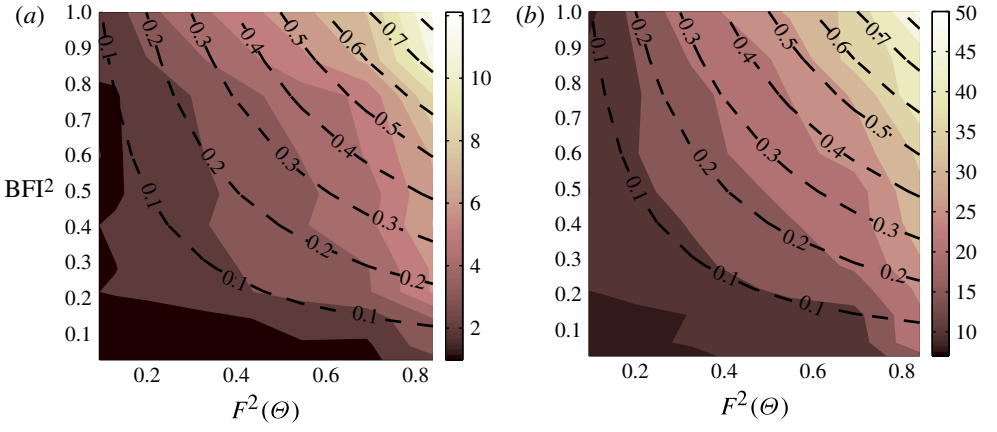

FIGURE 20. (Colour online) Contour plots (greyscale/colours) of (*a*) $P_N^{\max}/P_R$ and (*b*) $P_A^{\max}/P_R$ as a function of BFI^2 and $F^2(\Theta)$. The dashed lines are the contours of MBFI^2.

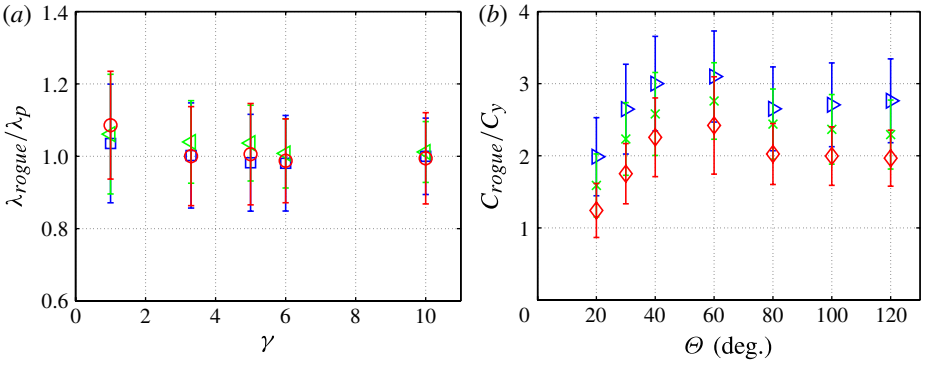

FIGURE 21. (Colour online) (*a*) Average rogue wavelength λ_{rogue} as a function of spectral bandwidth for wave fields $\varepsilon = 0.14$, and $\Theta = 20°$ (◯), 40° (□) and 80° (◁). (*b*) Average rogue wave crest length C_{rogue} relative to the average crest length C_y of the initial wave field as a function of spreading angle Θ for wave fields $\varepsilon = 0.14$, and $\gamma = 1$ (▷), 5 (×) and 10 (◇). Average crest length $C_y = \lambda_y/2 = \pi/\langle k_y^2 \rangle^{1/2}$. The error bars indicate one standard deviation.

5. Geometric characteristics of rogue waves

Not only does the identification of rogue waves from MIT-Wave give their occurrence probability, but also the HOS direct simulations provide detailed information on the geometry and kinematics (surface elevation, velocity and pressure fields) of such events. As a preliminary investigation, we consider the geometric features of rogue waves and wave groups in terms of their wavelength, crest length, area size and group structure, and dependence of these on the (initial) spectral parameters.

5.1. *Geometric features of rogue waves*

Once a rogue wave, in particular the crest and trough pair associated with H ($\geqslant \alpha H_s$) (hereafter referred to as the 'main' wave), is identified in a general directional wave field (§ 4.1), we define the wavelength of the rogue wave λ_{rogue} as the distance between the two adjacent zero up-crossing points along a line parallel to the dominant direction containing the crest point $\boldsymbol{x}_c$. Similarly, a crest length C_{rogue} is defined as the distance between two adjacent zero crossing points along a line perpendicular to the dominant direction containing the crest point $\boldsymbol{x}_c$. Rogue waves are reported to appear as an isolated large wave or as a dominant wave within a large wave group (Kharif & Pelinovsky 2003). To characterize this, we repeat § 4.1 but now use a new 'group' threshold $H/H_s = \alpha_G$ ($<\alpha$, typically), identifying all the $\mathscr{R} = \mathscr{R}_G$ for this threshold value. For given α and α_G, a rogue wave group is identified if any of the $\mathscr{R}_G$ overlaps and the union of the $\mathscr{R}_G$ contains a main wave satisfying $H/H_s \geqslant \alpha$. In this case, we say that this is a rogue wave group of 'n' waves (hereafter G_n) if n overlapping $\mathscr{R}_G$ are involved. Note that this definition/procedure is general for arbitrary directionally spread wave fields, and the number n does not distinguish among the different configurations (or positions) of $\mathscr{R}_G$ in such groups.

5.1.1. *Wave length and crest length of rogue waves*

For the rogue waves identified in MIT-Wave (with $\alpha = 2$), figure 21(*a*) shows the average wavelength of rogue waves over the evolution time $0 \leqslant t/T_p \leqslant 150$ as a function of spectral bandwidth (γ) for wave fields with a range of spreading

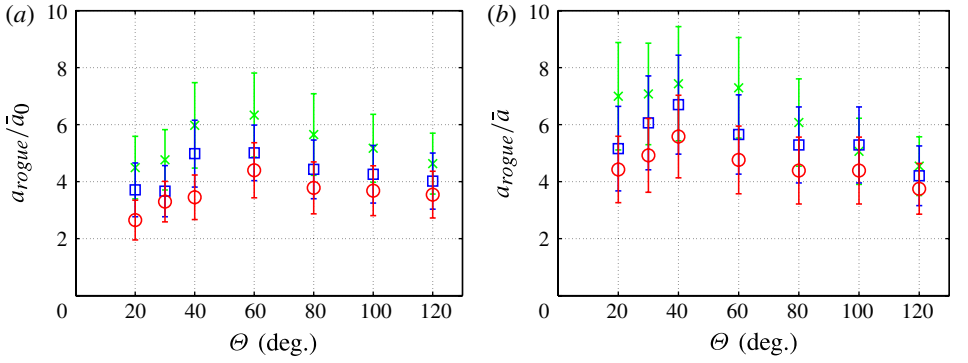

FIGURE 22. (Colour online) The average rogue wave area a_{rogue}, (*a*) scaled by the average area of initial wave fields $\bar{a}_0$, and (*b*) relative to the average wave area $\bar{a} = \lambda_x\lambda_y/\sqrt{2\pi}$ of the wave fields, as a function of spreading angles, for directional wave fields with $\varepsilon = 0.14$, and $\gamma = 1$ (×), 5 (□) and 10 (○). The error bars indicate one standard deviation during the evolution time considered.

angles. We observe that, for the broad range of spreading angles considered, λ_{rogue} is comparable to the peak wavelength λ_p. This gives further support to the suggestion that the dominant mechanism is MI around the peak wavenumber over slowly varying space/time. For wave fields with broad-band frequency spectrum (small γ), the average rogue wavelength $\bar{\lambda}_{rogue}$ is slightly longer than λ_p, especially for small spreading angle, where $\bar{\lambda}_{rogue} \approx 1.1\lambda_p$. With increasing spectral bandwidth, the standard deviation of λ_{rogue} increases. The dependence of λ_{rogue} on the spreading angle is rather subtle. There is a tendency for λ_{rogue} to be slightly greater in wave fields with large spreading angles, although the difference is much smaller than the standard deviation. Figure 21(*b*) shows the average crest length of rogue waves $\bar{C}_{rogue}$ over the time considered relative to the average crest length C_y of the initial wave fields as a function of spreading angles. For wave fields with small spreading angles, $\bar{C}_{rogue}/C_y$ increases with increasing Θ. As the spreading angle becomes large, $\bar{C}_{rogue}/C_y$ is nearly constant. Given the spreading angle, $\bar{C}_{rogue}/C_y$ increases as the spectral bandwidth increases. For short-crested wave fields with $\Theta \geqslant 60°$, the average crest length of rogue waves is considerably greater than the average crest length of the initial wave fields ($\bar{C}_{rogue}/C_y > 2$).

5.1.2. *Area size of rogue waves*

Figure 22(*a*) shows the average size of rogue waves $\bar{a}_{rogue}$ (§ 4.3), scaled by the average wave size of the initial wave field $\bar{a}_0$, as a function of spreading angle and spectral bandwidth. In the range of relatively small $\Theta \lesssim 60°$, $\bar{a}_{rogue}/\bar{a}_0$ increases as Θ increases. For larger Θ, $\bar{a}_{rogue}/\bar{a}_0$ slowly decreases as Θ increases. For given Θ, $\bar{a}_{rogue}/\bar{a}_0$ increases as the spectral bandwidth increases (γ decreases). As the wave field evolves, the average size of waves $\bar{a}$ varies with time. Figure 22(*b*) shows $\bar{a}_{rogue}/\bar{a}$, which is the average of $a_{rogue}/\bar{a}(t)$ over time $0 \leqslant t \leqslant 150T_p$, as a function of Θ and γ. Comparing figures 22(*a*) and 22(*b*), $\bar{a}_{rogue}/\bar{a}$ behaves similarly to $\bar{a}_{rogue}/\bar{a}_0$ but with a larger value. The large standard deviation in the range of small Θ is associated with a significant change of the underlying spectrum due to the MI effect.

5.1.3. *Grouping of rogue waves*

For given $\alpha = 2$ and $\alpha_G = 1.8$, we catalogue the rogue wave groups G_n obtained from MIT-Wave. Figure 23 shows the percentages of G_2 and G_3 rogue wave groups,

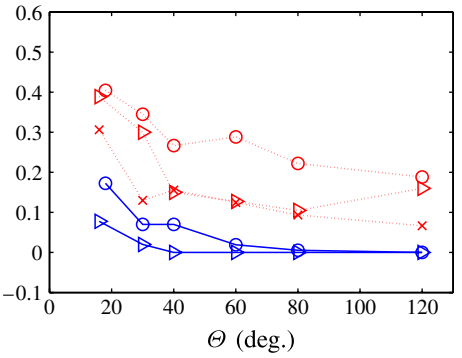

FIGURE 23. (Colour online) Percentage of rogue wave groups, $G_2\,\%$ (· · · · · ·) and $G_3\,\%$ (——), as functions of spreading angle for wave fields with steepness $\varepsilon = 0.14$, and $\gamma = 1$ (×), 5 (▷) and 10 (◯). Results are obtained using $\alpha_G = 1.8$ and $\alpha = 2$.

denoted as $G_2\,\%$ and $G_3\,\%$, among the rogue wave populations. For a given spectral bandwidth, both $G_2\,\%$ and $G_3\,\%$ decrease with increasing Θ for $\Theta \lesssim 60°$, while they are nearly independent of Θ for larger Θ. For a fixed Θ, both $G_2\,\%$ and $G_3\,\%$ increase as γ increases. These observations are consistent with the effect of MI on rogue wave development.

5.2. *Analysis of rogue wave shapes using proper orthogonal decomposition*

A large number of rogue waves obtained for a broad range of spectral parameters are found to have surprisingly similar geometric features. To identify these salient features, and to see if they can be represented by a relatively small number of parameters, we analyse rogue wave surface profiles in MIT-Wave by applying the proper orthogonal decomposition (POD), which provides a statistical method to obtain a compact representation of the data to extract the dominant structures.

The general analysis of rogue wave groups that contain large n waves involving different possible configurations is complex. As a preliminary investigation, we focus on the relatively simple case of G_1, i.e. a single large (3D) wave satisfying $H \geqslant \alpha H_s$.

We first consider unidirectional waves and write the POD expansion of the rogue wave as

$$\eta_{rogue}(\hat{x})/H_s = \eta_{POD}(\hat{x}) = \sum_{m=1}^{M_x} C_m U_m(\hat{x};\varepsilon,\gamma), \quad 0 \leqslant \hat{x} \leqslant 1, \tag{5.1}$$

where $\hat{x} = x/\Lambda_r$, and Λ_r is the length of the rogue wave defined as the distance between the down-crossing of the up-wave trough and the up-crossing of the down-wave trough around the rogue wave crest. In (5.1), $U_m(\hat{x};\varepsilon,\gamma)$ is the mth POD mode for wave fields with spectral parameters ε and γ; C_m is the coefficient of the mth POD mode; and M_x the total mode number. The U_m, $m = 1, 2, \ldots,$ form orthogonal basis vectors that characterize the ensemble of rogue wave shapes. The rogue wave profiles are selected from HOS simulations with time interval $\Delta T = 10T_p$. To compute U_m, we typically use $O(1000)$ rogue wave profiles from MIT-Wave (the difference in U_m obtained using a larger ensemble is less than 1 %). Note that, unlike the rogue wave probability, POD shapes are not invariant if crest and trough are interchanged in the above procedure. For uniqueness of POD shapes, we have chosen to describe rogue

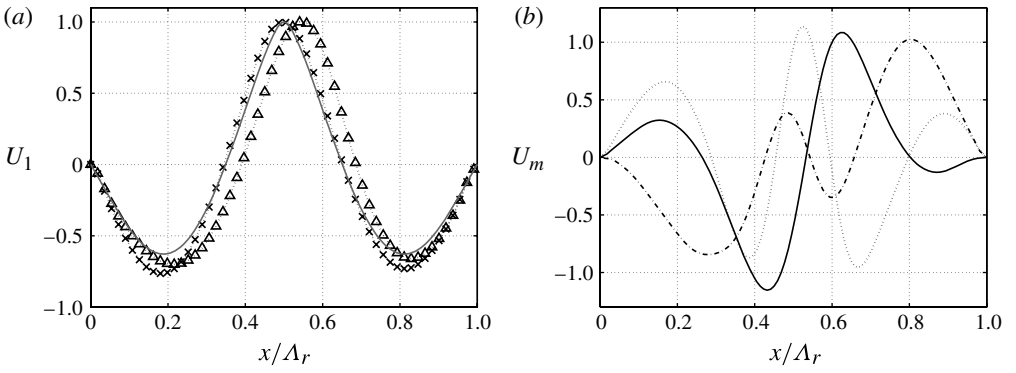

FIGURE 24. (*a*) Plot of $U_1(x)$ for unidirectional wave fields with $\gamma = 6$, and $\varepsilon = 0.07$ ($\cdots \times \cdots$) and $\varepsilon = 0.14$ ($\cdots \triangle \cdots$). The autocovariance function $\rho(x)$ is also shown (——). (*b*) Plot of U_m for unidirectional wave fields with $\varepsilon = 0.14$ and $\gamma = 6$ for $m = 2$ (——), $m = 3$ (- - - -) and $m = 4$ ($\cdots\cdots$). Waves propagate from left to right.

waves in the 'crest-centred' profile. To obtain POD shapes of rogue waves described in the 'trough-centred' profile, similar approaches can be applied.

Figure 24(*a*) shows the leading POD mode U_1 of G_1 rogue waves for unidirectional wave fields with different spectral steepness ε. We observe that U_1 has a sharp crest and two shallow troughs, indicating the nonlinearity of the wave. In addition, U_1 is asymmetric with respect to the crest and the crest is skewed to the up-wave trough (i.e. right trough in the figure with wave propagation to the right). The down-wave trough is slightly deeper than the up-wave trough, which suggests that more rogue waves may be identified if the up-crossing approach is used in analysing time series. This is consistent with the observations in Pinho *et al.* (2004). With increasing steepness, U_1 becomes more asymmetric and skewed, suggesting more significant nonlinearity of the rogue waves. This mode profile can be contrasted to the average profile around a local extreme crest for linear Gaussian waves, which is proportional to the autocovariance function, $\rho(x) = \int_k \cos(kx)\Psi(k)\,\mathrm{d}k / \int_k \Psi(k)\,\mathrm{d}k$, where $\Psi(k)$ is the wavenumber spectrum (Lindgren 1970; Boccotti 1983). In comparison with $\rho(x)$, U_1 has shallower up-wave trough and deeper down-wave trough, while $\rho(x)$ is symmetric with respect to the wave crest. Figure 24(*b*) plots the profile of the higher-order POD modes U_m, $m = 2, 3, 4$. These U_m describe the perturbations of rogue wave profiles around the leading mode U_1. Higher POD modes are more oscillatory, describing perturbations with successively shorter scales.

It is more interesting to distinguish the rogue waves with crest greater (less) than trough, i.e. a 'wall of water' ('deep hole'), and to name them as crest-dominant (trough-dominant) rogue waves. We find that crest-dominant rogue waves generally occur more frequently than trough-dominant rogue waves. The first POD modes of crest- and trough-dominant rogue waves are shown in figure 25. For the trough-dominant rogue waves, a trough-centre profile is used. Similarly to figure 24(*a*), U_1 becomes more asymmetric and skewed for both crest- and trough-dominant rogue waves as the wave steepness increases.

Figure 26(*a*) shows the coefficients of POD modes C_m for wave fields with a range of spectral bandwidths. The magnitudes of the coefficients decrease rapidly and only the first mode has a non-zero mean. The standard deviation of the coefficients decreases for the higher modes. This suggests that the dominant geometry of the rogue

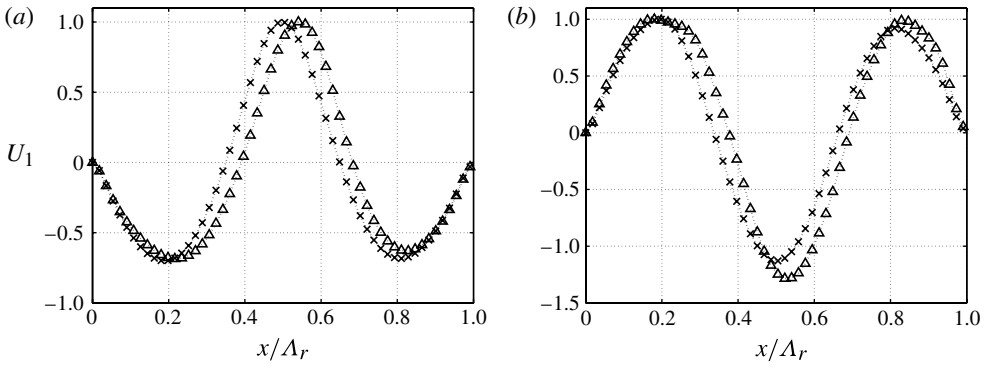

FIGURE 25. Leading POD mode $U_1(x)$ for (a) crest-dominant and (b) trough-dominant rogue waves. Unidirectional wave fields with $\gamma = 6$, and $\varepsilon = 0.07$ ($\cdots \times \cdots$, 710 crest- and 290 trough-dominant rogue waves) or $\varepsilon = 0.14$ ($\cdots \triangle \cdots$, 914 crest- and 86 trough-dominant rogue waves). Waves propagate from left to right.

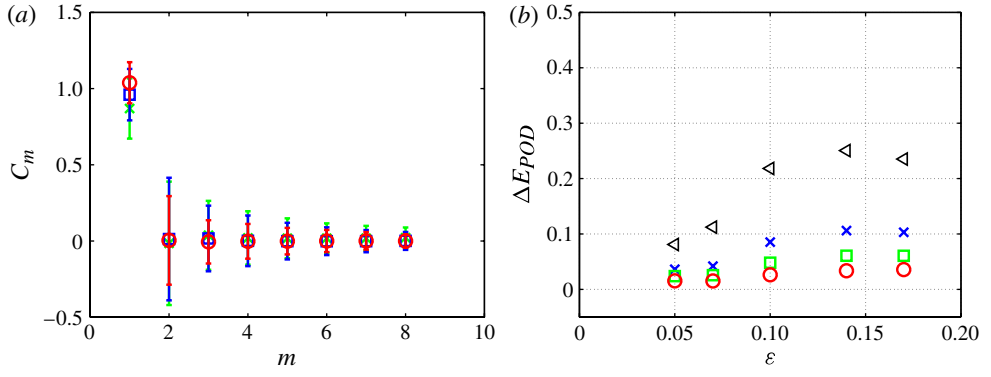

FIGURE 26. (Colour online) (a) Coefficients of POD modes C_m, $m = 1, \ldots, 8$, for unidirectional wave fields with $\gamma = 5$, and $\varepsilon = 0.07$ (○), 0.1 (□) and 0.14 (×). The error bars indicate one standard deviation. (b) The average error of POD approximations ΔE_{POD} using M_x POD modes: $M_x = 1$ (◁), 2 (×), 3 (□) and 4 (○).

wave profile η/H_s can be reasonably approximated using only U_1. The representation error of POD is defined as $\Delta E_{POD} = |E_{POD} - E_R|/E_R$, where $E_R = \int \eta^2_{\text{rogue}}\,\mathrm{d}x$ and $E_{\text{POD}} = \int \eta^2_{\text{POD}}\,\mathrm{d}x$. Figure 26($b$) shows the average representation error of POD modes for wave fields with a broad range of steepness. For relatively small steepness $\varepsilon < 0.1$, the errors are within 20 % using only U_1. For wave fields with greater steepness, more modes are needed to achieve a satisfactory accuracy. The error decreases as more POD modes are used. For a broad range of wave-field steepness, when $M_x = 4$ POD modes are used, the mean representation error ΔE_{POD} is less than 5 %.

The foregoing can be extended to 3D large waves in a straightforward manner. For directional wave fields, the POD representations of rogue waves η_{rogue} are written in the form

$$\eta_{rogue}(\hat{x}, \hat{y})/H_s = \eta_{POD}(\hat{x}, \hat{y}) = \sum_{n}^{M_y} \sum_{m}^{M_x} C_{m,n} U_m(\hat{x}) V_n(\hat{y}), \tag{5.2}$$

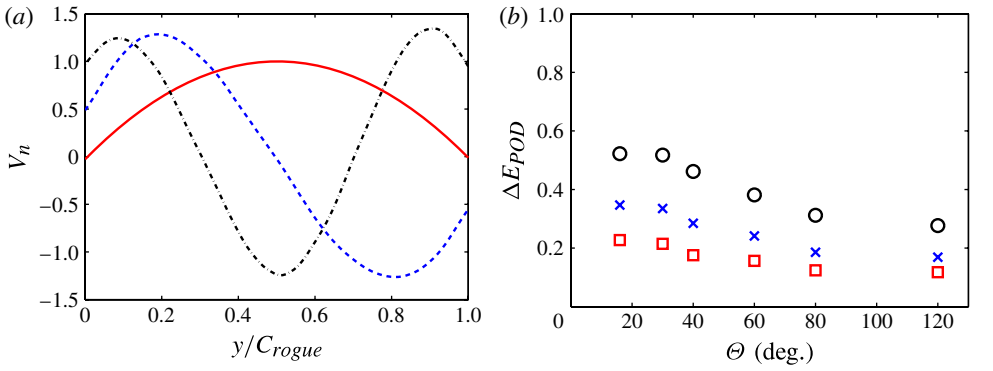

FIGURE 27. (Colour online) (*a*) POD modes in the y direction, V_n, with $n = 1$ (—), 2 (- - -) and 3 (- · -), for directional wave field $\varepsilon = 0.1$, $\gamma = 5$ and $\Theta = 60°$. (*b*) Average error of POD representations ΔE_{POD} using $M_x = 1$, $M_y = 1$(◯), $M_x = 2$, $M_y = 2$ (×) and $M_x = 3$, $M_y = 3$ (□).

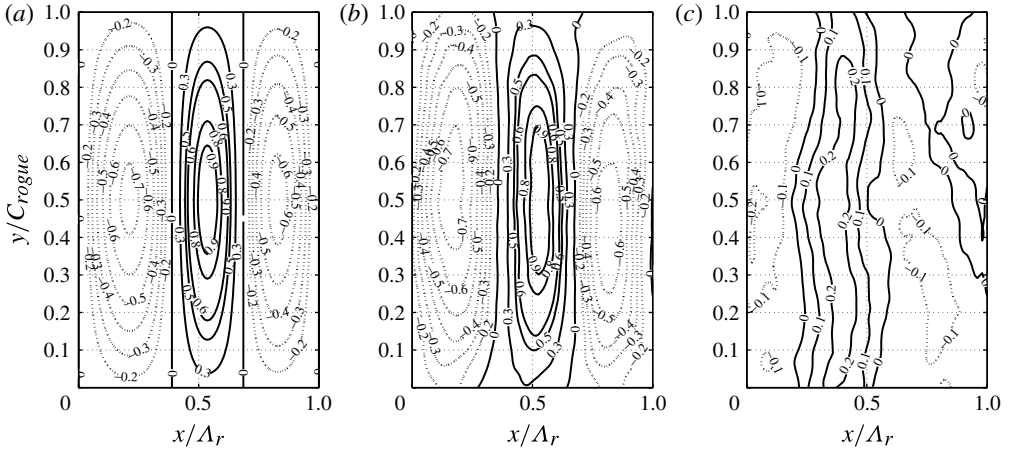

FIGURE 28. (*a*) Leading POD mode $U_1(\hat{x})V_1(\hat{y})$ in (5.2), (*b*) $W_1(\hat{x}, \hat{y})$ in (5.3) and (*c*) $W_1(\hat{x}, \hat{y}) - U_1(\hat{x})V_1(\hat{y})$ for rogue waves in the directional wave field $\varepsilon = 0.1$, $\gamma = 5$ and $\Theta = 60°$. The POD modes are obtained based on a sample size of 200. Waves propagate from left to right.

where $\hat{x} = x/\Lambda_r$ and $\hat{y} = y/C_{rogue}$; $U_m(\hat{x})$ and $V_n(\hat{y})$ are the POD modes in the x and y directions; and M_x and M_y are the number of POD modes in the two horizontal directions. For simplicity, we assume that $U_m(\hat{x})$ in (5.2) is given by (5.1), and we focus on the transverse modulations $V_n(\hat{y})$. Plots of V_n, $n = 1, 2, 3$, obtained from $O(200)$ 3D rogue waves (collected from HOS simulations with time interval $\Delta T = 10T_p$) are shown in figure 27(*a*). We can see that V_1, the leading-order along-crest modulation (scaled by C_{rogue}), is positive definite and quite symmetric (after $N_{rogue} = 200$) with respect to y_c. The higher-order transverse POD modes $V_{2,3}$ describe successively shorter modulations with both positive and negative values and are generally not symmetric (relative to y_c). Figure 28(*b*) shows the average accuracy of the POD expressions of rogue waves for wave fields with different initial spreading angles. The error of the POD representation decreases as the spreading angle increases.

Over the broad range of Θ, the average errors of POD representation using only the three leading-order POD modes in each direction ($M_x = M_y = 3$) are less than 20 %.

To assess the assumptions inherent in (5.2), we can alternatively represent η_{rogue} using 2D POD modes as

$$\eta_{rogue}(\hat{x}, \hat{y})/H_s = \eta_{POD}(\hat{x}, \hat{y}) = \sum_{m=1}^{M_{xy}} C_m W_m(\hat{x}, \hat{y}; \varepsilon, \gamma, \Theta), \tag{5.3}$$

where M_{xy} is the number of 2D POD modes and $W_m(\hat{x}, \hat{y}; \varepsilon, \gamma, \Theta)$ is the mth 2D POD mode for directional wave fields specified by ε, γ and Θ. Figure 28 plots the contours of $W_1(\hat{x}, \hat{y})$ as compared to $U_1(\hat{x})V_1(\hat{y})$ from (5.2) and (5.3), respectively. Qualitatively, W_1 and U_1V_1 are very similar; however, W_1 is less asymmetric than U_1V_1 in both the longitudinal and transverse directions. The quantitative differences between W_1 and U_1V_1 (figure 28*c*) are mainly in the shallower up-wave and down-wave troughs of U_1V_1 relative to W_1, which are consistent with the reduction effect of directional spreading on the nonlinearity of wave fields.

We remark that the efficacy of POD with only a few modes in describing the rogue wave geometries that we obtain is partly because only G_1 rogue waves (containing a single main wave) are considered, for which our finding might indeed be expected. With sufficiently large ensembles of rogue wave groups in MIT-Wave, the overall methodology applies equally to general G_n, but is not undertaken here.

6. Conclusion

We study the occurrence and dynamics of rogue waves in three-dimensional nonlinear deep-water wave fields using direct simulations based on a high-order spectral (HOS) method. Consistent with modulational instability (MI) of nonlinear waves, which is our main focus, we consider spatial domains $\mathscr{L} \times \mathscr{L}$ and evolution times $\mathscr{T}$, where $\mathscr{L}/\lambda_p, \mathscr{T}/T_p \sim O(\varepsilon^{-2})$ for our simulations. A large number $O(200)$ of 3D nonlinear HOS wave fields (MIT-Wave dataset) are generated using initial (JONSWAP) spectra with a broad range of spectral parameters. The accuracy and reliability of using HOS simulations in describing the nonlinear wave statistics are demonstrated by direct comparisons with wave basin experiments.

To assess the range of applicability of the NLS-type approach, we obtain results using the slightly broad-band modified NLS (BMNLS) model and compare and contrast these with HOS results. In general, BMNLS and HOS give qualitatively similar results for the initial time. For $\mathscr{L}/\lambda_p, \mathscr{T}/T_p \sim O(\varepsilon^{-2})$ and initially narrow frequency and directional spread wave fields, however, HOS obtains statistically quasi-stationary nonlinear non-Gaussian states after the broadening of the spectra. This is not predicted by BMNLS, which in general obtains monotonic spreading of energy to shorter and more directionally spreading waves, and almost Gaussian asymptotic statistics. As a result, BMNLS generally underpredicts the occurrence of rogue waves for longer times.

We elucidate the importance of MI in the evolution of directional wave fields using extensive HOS simulations. For wave fields with small spreading angles, MI leads to significant spectral broadening, strongly non-Gaussian wave statistics and enhanced probability of rogue waves. For wave fields with large spreading angles, the importance of MI is less significant, and the wave statistics are closer to Gaussian. For general directional spread wave fields, the occurrence probability based on the number of rogue waves P_N becomes problematic as crest lengths become short. The

problem is exacerbated since even initially narrowly spread seas become directionally broadened in the nonlinear evolution. To overcome this, we introduce the definition of *area* probability of rogue wave occurrence P_A, which is well defined and convergent for arbitrary 3D wave fields. We confirm the general correlation between both P_N and P_A and kurtosis. For relatively narrow spread seas, kurtosis, and hence occurrence probability, can be reasonably well predicted by the (initial) BFI of the wave field. This is no longer true for broad directionally spreading wave fields. We propose a modified Benjamin–Feir index (MBFI) that accounts for directional spreading and show that kurtosis, P_N and P_A are well predicted by MBFI over a broad range of spectral nonlinearity, frequency bandwidth and directional spreading. HOS not only obtains the rogue wave events but also provides the detailed geometry and kinematics within the wave field. Using the substantial catalogue of rogue waves in MIT-Wave, we investigate the geometric structures of such waves and their dependence on the underlying wave spectra. We analyse the shapes of 2D and 3D rogue waves using proper orthogonal decomposition (POD) and find that, in general, for rogue waves containing a single main wave, the wave profile can be well represented using a few leading POD modes.

As an initial study, our main focus is on the effects of MI on the formation of rogue waves. Based on this, we conduct direct HOS simulations covering the requisite spatial and temporal scales using nonlinear order $M = 3$. While the simulation scales are already large, these do not address how mechanisms and significant interactions over even greater scales (e.g. McLean 1982) might modify our findings. At these greater scales, effects ignored in the present study such as input from wind (at even moderate speeds) (Lavrenov 1998; Abdalla & Cavaleri 2002; Dysthe *et al.* 2003; Kharif *et al.* 2007) could also play appreciable roles.

Acknowledgements

This research is supported financially by grants from the Office of Naval Research. Large-scale simulations and compilation of the MIT-Wave dataset are made possible by Challenge grants from the High Performance Computing Modernization Program (HPCMP).

REFERENCES

ABDALLA, S. & CAVALERI, L. 2002 Effect of wind variability and variable air density on wave modelling. *J. Geophys. Res.* **107** (C7), 3080.

ALBER, I. E. 1978 The effects of randomness on the stability of two-dimensional surface wavetrains. *Proc. R. Soc. Lond.* A. **363**, 525–546.

ANNENKOV, S. Y. & SHRIRA, V. I. 2009*a* Evolution of kurtosis for wind waves. *Geophys. Res. Lett.* **36**, L13603.

ANNENKOV, S. Y & SHRIRA, V. I. 2009*b* Fast nonlinear evolution in wave turbulence. *Phys. Rev. Lett.* **102** (2), 24502.

BATEMAN, W. J. D., SWAN, C. & TAYLOR, P. H. 2001 On the efficient numerical simulation of directionally spread surface water waves. *J. Comput. Phys.* **174** (1), 277–305.

BENJAMIN, T. B. & FEIR, J. E. 1967 The disintegration of wave trains in deep water. Part 1. Theory. *J. Fluid Mech.* **27** (3), 417–430.

BOCCOTTI, P. 1983 Some new results on statistical properties of wind waves. *Appl. Ocean Res.* **5** (3), 134–140.

CHALIKOV, D. 2009 Freak waves: their occurrence and probability. *Phys. Fluids* **21**, 076602.

CLAMOND, D., FRANCIUS, M., GRUE, J. & KHARIF, C. 2006 Long time interaction of envelope solitons and freak wave formations. *Eur. J. Mech.* (B/*Fluids)* **25**, 536–553.

DOMMERMUTH, D. 2000 The initialization of nonlinear waves using an adjustment scheme. *Wave Motion* **32** (4), 307–317.

DOMMERMUTH, D. & YUE, D. K. P. 1987 A higher-order spectral method for the study of nonlinear gravity waves. *J. Fluid Mech.* **184**, 267–288.

DOMMERMUTH, D. & YUE, D. K. P. 1988 The nonlinear three-dimensional waves generated by a moving surface disturbance. In *Proceedings of 17th Symposium on Naval Hydrodynamics, The Hague, The Netherlands*.

DYSTHE, K. B. 1979 Note on a modification to the nonlinear Schrödinger equation for application to deep water waves. *Proc. R. Soc. Lond.* A **369** (1736), 105–114.

DYSTHE, K. B., KROGSTAD, H. E. & MULLER, P. 2008 Oceanic rogue waves. *Annu. Rev. Fluid Mech.* **40**, 287–310.

DYSTHE, K. B., TRULSEN, K., KROGSTAD, H. E. & SOCQUET-JUGLARD, H. 2003 Evolution of a narrow-band spectrum of random surface gravity waves. *J. Fluid Mech.* **478**, 1–10.

FORRISTALL, G. Z. 2000 Wave crest distributions: observations and second-order theory. *J. Phys. Oceanogr.* **30** (8), 1931–1943.

FORRISTALL, G. Z. 2005 Understanding rogue waves: are new physics really necessary? In *Rogue Waves: Proceedings of the 14th 'Aha Huliko'a Hawaiian Winter Workshop, Honolulu, HI*, pp. 29–35.

GEMMRICH, J. R. & FARMER, D. M. 1999 Observations of the scale and occurrence of breaking surface waves. *J. Phys. Oceanogr.* **29** (10), 2595–2606.

GRAMSTAD, O. & TRULSEN, K. 2007 Influence of crest and group length on the occurrence of freak waves. *J. Fluid Mech.* **582**, 463–472.

GUEDES SOARES, C., CHERNEVA, Z. & ANTÃO, E. M. 2003 Characteristics of abnormal waves in North Sea storm sea states. *Appl. Ocean Res.* **25** (6), 337–344.

HWANG, P. A., WANG, D. W., WALSH, E. J., KRABILL, W. B. & SWIFT, R. N. 2000 Airborne measurements of the wavenumber spectra of ocean surface waves. Part II: directional distribution. *J. Phys. Oceanogr.* **30** (11), 2768–2787.

JANSSEN, P. A. E. M. 2003 Nonlinear four-wave interactions and freak waves. *J. Phys. Oceanogr.* **33** (4), 863–884.

JANSSEN, P. A. E. M. 2009 On some consequences of the canonical transformation in the Hamiltonian theory of water waves. *J. Fluid Mech.* **637**, 1–44.

KHARIF, C., GIOVANANGELI, J. P., TOUBOUL, J., GRARE, L. & PELINOVSKY, E. 2007 Influence of wind on extreme wave events: experimental and numerical approaches. *J. Fluid Mech.* **594**, 209–247.

KHARIF, C. & PELINOVSKY, E. 2003 Physical mechanisms of the rogue wave phenomenon. *Eur. J. Mech. (B/Fluids)* **22** (6), 603–634.

KHARIF, C., PELINOVSKY, E. & SLUNYAEV, A. 2009 *Rogue Waves in the Ocean*. Springer.

LAVRENOV, I. V. 1998 The wave energy concentration at the Agulhas Current off South Africa. *Natural Hazards* **17** (2), 117–127.

LAWTON, G. 2001 Monsters of the deep (the perfect wave). *New Sci.* **170** (2297), 28–32.

LINDGREN, G. 1970 Some properties of a normal process near a local maximum. *Ann. Math. Statist.* **41** (6), 1870–1883.

LIU, Y. & YUE, D. K. P. 1998 On generalized Bragg scattering of surface waves by bottom ripples. *J. Fluid Mech.* **356**, 297–326.

LO, E. & MEI, C. C. 1985 A numerical study of water-wave modulation based on a higher-order nonlinear Schrödinger equation. *J. Fluid Mech.* **150**, 395–416.

LONGUET-HIGGINS, M. S. 1952 On the statistical distribution of the heights of sea waves. *J. Mar. Res.* **11** (3), 245–266.

LONGUET-HIGGINS, M. S. 1963 The effect of nonlinearities on statistical distribution in the theory of sea waves. *J. Fluid Mech.* **17**, 459–480.

MCLEAN, J. W. 1982 Instabilities of finite-amplitude gravity waves on water of finite depth. *J. Fluid Mech.* **114**, 331–341.

MORI, N. & JANSSEN, P. A. E. M. 2006 On kurtosis and occurrence probability of freak waves. *J. Phys. Oceanogr.* **36** (7), 1471–1483.

MORI, N., ONORATO, M. & JANSSEN, P. A. E. M. 2011 On the estimation of the kurtosis in directional sea states for freak wave forecasting. *J. Phys. Oceanogr.* **41** (8), 1484–1497.

MORI, N. & YASUDA, T. 2002 A weakly non-Gaussian model of wave height distribution for random wave train. *Ocean Engng* **29** (10), 1219–1231.

ONORATO, M., CAVALERI, L., FOUQUES, S., GRAMSTAD, O., JANSSEN, P. A. E. M., MONBALIU, J., OSBORNE, A. R., PAKOZDI, C., SERIO, M., STANSBERG, C. T., TOFFOLI, A. & TRULSEN, K. 2009 Statistical properties of mechanically generated surface gravity waves: a laboratory experiment in a three-dimensional wave basin. *J. Fluid Mech.* **627**, 235–257.

ONORATO, M., CAVALERI, L., GRAMSTAD, O., JANSSEN, P. A. E. M., MONBALIU, J., OSBORNE, A. R., SERIO, M., STANSBERG, C. T., TOFFOLI, A. & TRULSEN, K. 2008 Statistical properties of mechanically generated surface gravity waves: a laboratory experiment in a 3D wave basin. In *Rogue Waves 2008, Brest, France*.

ONORATO, M., OSBORNE, A. R. & SERIO, M. 2002 Extreme wave events in directional, random oceanic sea states. *Phys. Fluids* **14** (4), L25–L28.

ONORATO, M., OSBORNE, A. R., SERIO, M. & BERTONE, S. 2001 Freak waves in random oceanic sea states. *Phys. Rev. Lett.* **86** (25), 5831–5834.

ONORATO, M., OSBORNE, A. R., SERIO, M., CAVALERI, L., BRANDINI, C. & STANSBERG, C. T. 2004 Observation of strongly non-Gaussian statistics for random sea surface gravity waves in wave flume experiments. *Phys. Rev.* E **70** (6), 067302.

PINHO, U. F., LIU, P. C. & RIBEIRA, C. E. P. 2004 Freak waves at Campos Basin, Brazil. *Geofizika* **21**, 53–66.

PITERBARG, V. I. 1996 *Asymptotic Methods in the Theory of Gaussian Processes and Fields*, Translations of Mathematical Monographs, vol. 148. American Mathematical Society.

RAPP, R. J. & MELVILLE, W. K. 1990 Laboratory measurements of deep-water breaking waves. *Phil. Trans. R. Soc. Lond.* A **331** (1622), 735–800.

RUBAN, V. P. 2011 Enhanced rise of rogue waves in slant wave groups. *JETP Lett.* **94** (3), 177–181.

SEGUR, H., HENDERSON, D., CARTER, J., HAMMACK, J., LI, C.-M., PHEIFF, D. & SOCHA, K. 2005 Stabilizing the Benjamin–Feir instability. *J. Fluid Mech.* **539**, 229–271.

SHEMER, L., KIT, E. & JIAO, H. 2002 An experimental and numerical study of the spatial evolution of unidirectional nonlinear water-wave groups. *Phys. Fluids* **14**, 3380.

SHEMER, L. & SERGEEVA, A. 2009 An experimental study of spatial evolution of statistical parameters in a unidirectional narrow-banded random wavefield. *J. Geophys. Res.* **114** (C1), C01015.

SHEMER, L., SERGEEVA, A. & LIBERZON, D. 2010*a* Effect of the initial spectrum on the spatial evolution of statistics of unidirectional nonlinear random waves. *J. Geophys. Res.* **115** (C12), C12039.

SHEMER, L., SERGEEVA, A. & SLUNYAEV, A. 2010*b* Applicability of envelope model equations for simulation of narrow-spectrum unidirectional random wave field evolution: experimental validation. *Phys. Fluids* **22**, 016601.

SKOURUP, J., HANSEN, N. E. O. & ANDREASEN, K. K. 1997 Non-Gaussian extreme waves in the central North Sea. *J. Offshore Mech. Arctic Engng* **119** (3), 146–150.

SLUNYAEV, A., DIDENKULOVA, I. & PELINOVSKY, E. 2011 Rogue waters. *Contemp. Phys.* **52** (6), 571–590.

SLUNYAEV, A. V. & SERGEEVA, A. V. 2011 Stochastic simulation of unidirectional intense waves in deep water applied to rogue waves. *JETP Lett.* **94** (10), 779–786.

SOCQUET-JUGLARD, H., DYSTHE, K., TRULSEN, K., KROGSTAD, H. E. & LIU, J. 2005 Probability distributions of surface gravity waves during spectral changes. *J. Fluid Mech.* **542**, 195–216.

STANSBERG, C. T. 1994 Effects from directionality and spectral bandwidth on nonlinear spatial modulations of deep-water surface gravity wave trains. In *Proceedings of the 24th International Conference on Coastal Engineering, Kobe, Japan*, vol. 1, pp. 579–593. ASCE.

STANSELL, P. 2005 Distributions of extreme wave, crest and trough heights measured in the North Sea. *Ocean Engng* **32** (8–9), 1015–1036.

STOCKER, J. R. & PEREGRINE, D. H. 1999 The current-modified nonlinear Schrödinger equation. *J. Fluid Mech.* **399**, 335–353.

TAYFUN, M. A. 1980 Narrow-band nonlinear sea waves. *J. Geophys. Res.* **85** (C3), 1548–1552.

TOFFOLI, A., CAVALERI, L., BABANIN, A. V., BENOIT, M., BITNER-GREGERSEN, E. M., MONBALIU, J., ONORATO, M., OSBORNE, A. R. & STANSBERG, C. T. 2011 Occurrence of extreme waves in three-dimensional mechanically generated wave fields propagating over an oblique current. *Nat. Hazards Earth Syst. Sci.* **11**, 895–903.

TOFFOLI, A., GRAMSTAD, O., TRULSEN, K., MONBALIU, J., BITNER-GREGERSEN, E. & ONORATO, M. 2010 Evolution of weakly nonlinear random directional waves: laboratory experiments and numerical simulations. *J. Fluid Mech.* **664**, 313–336.

TOFFOLI, A., LEFEVRE, J. M., BITNER-GREGERSEN, E. & MONBALIU, J. 2005 Towards the identification of warning criteria: analysis of a ship accident database. *Appl. Ocean Res.* **27** (6), 281–291.

TRULSEN, K. & DYSTHE, K. B. 1996 A modified nonlinear Schrödinger equation for broader bandwidth gravity waves on deep water. *Wave Motion* **24**, 281–289.

WASEDA, T., KINOSHITA, T. & TAMURA, H. 2009 Evolution of a random directional wave and freak wave occurrence. *J. Phys. Oceanogr.* **39** (3), 621–639.

WEST, B. J., BRUECKNER, K. A., JANDA, R. S., MILDER, D. M. & MILTON, R. L. 1987 A new numerical method for surface hydrodynamics. *J. Geophys. Res.* **92** (C11), 11803–11824.

WU, G. 2004 Direct simulation and deterministic prediction of large-scale nonlinear ocean wave-field. PhD thesis, Massachusetts Institute of Technology, Cambridge, MA.

WU, G., LIU, Y. & YUE, D. K. P. 2006 A note on stabilizing the Benjamin–Feir instability. *J. Fluid Mech.* **556**, 45–54.

XIAO, W. 2013 Study of directional ocean wavefield evolution and rogue wave occurrence using large-scale phase-resolved nonlinear simulations. PhD thesis, Massachusetts Institute of Technology, Cambridge, MA.

ZAKHAROV, V. E., DYACHENKO, A. I. & VASILYEV, O. A. 2002 New method for numerical simulation of a nonstationary potential flow of incompressible fluid with a free surface. *Eur. J. Mech. (*B*/Fluids)* **21** (3), 283–291.